IEA INTERNATIONAL ENERGY AGENCY

Characterization of the spatio-temporal variations and ramp rates of solar radiation and PV

Report of IEA Task 14 Subtask 1.3

PVPS

PHOTOVOLTAIC
POWER SYSTEMS
PROGRAMME

Report IEA PVPS T14-05:2015
ISBN: 978-3-906042-35-0

INTERNATIONAL ENERGY AGENCY
PHOTOVOLTAIC POWER SYSTEMS PROGRAMME

Characterization of the spatio-temporal variations and ramp rates of solar radiation and PV

IEA PVPS Task 14, Subtask 1.3
Report IEA-PVPS T14-05:2015
August 2015

ISBN
978-3-906042-35-0

Authors:

Jan Remund, jan.remund@meteotest.ch
Catarina Calhau, catarina.Calhau@edp.pt
Lionel Perret, lionel.perret@planair.ch
Davy Marcel, davy.marcel@planair.ch

Executive Summary

The increasing penetration of PV systems in the distribution network creates new opportunities but also raises several issues for the grid operation. New challenges, arising from the variable nature of solar energy generation, must be tackled in order to keep a stable and balanced power grid.

In this study, short term variability in power output due to changing intensity due to cloud cover is assessed for its impact on energy delivery. Studies on this subject conclude that while there may be local variability, there is a strong reduction in that variability when the aggregate of several PV systems is taken into account, rather than just one PV system. The analysis shows that the aggregated effect of many geographically dispersed systems PV systems yields a smoothing effect that reduces the impact of local variability.

Chapters two and three show the theoretical background of the smoothing effect. Three different variability methods are described: In the first one (representative blocks), the amplitude of the fluctuations was the main focus and information about the duration of the fluctuations was not considered. The second method (dispersion factor) focuses on the variability itself, but its data requisites were very demanding, which can be a hindrance. The third and final method (wavelet analysis) proved to be a good choice since it needs very limited data inputs and it is able to decompose the input irradiance signal into different timescales of fluctuations. By doing this, the variability reduction can be accessed and calculated separately for each timescale.

In the following chapters, the models are demonstrated in case studies for different regions and with different time and space resolution and one of a distributed generation system in Hawaii, USA.

The current report shows the general validity of the models and suggests a simple global model for modelling variability of PV fleets. Both need further validations at more sites and in more regions to detect the strengths and limitations of the models and the worldwide usability.

1. Introduction

The Earth receives 174 PW of incoming solar radiation at the upper atmosphere. Approximately 30% is reflected back to space while 20% is absorbed by clouds and atmosphere. As a result 50% of the solar energy reaches surface of the planet, which equals to 2.7 Mio. EJ per year. This amount is about five times as much as all of the Earth's total non-renewable resources of coal, oil, natural gas and mined uranium combined (0.53 Mio. EJ) [2] and 5'000 times higher than the world 's total energy consumption in 2012.

This energy can be used for many purposes, one of them being the conversion into electricity. The most common way of doing this is using photovoltaics (PV). Recently, the PV industry has witnessed a strong decrease in PV module prices. This strong decrease in prices facilitates and encourages an increasing deployment of PV systems (Fig. 1.1).

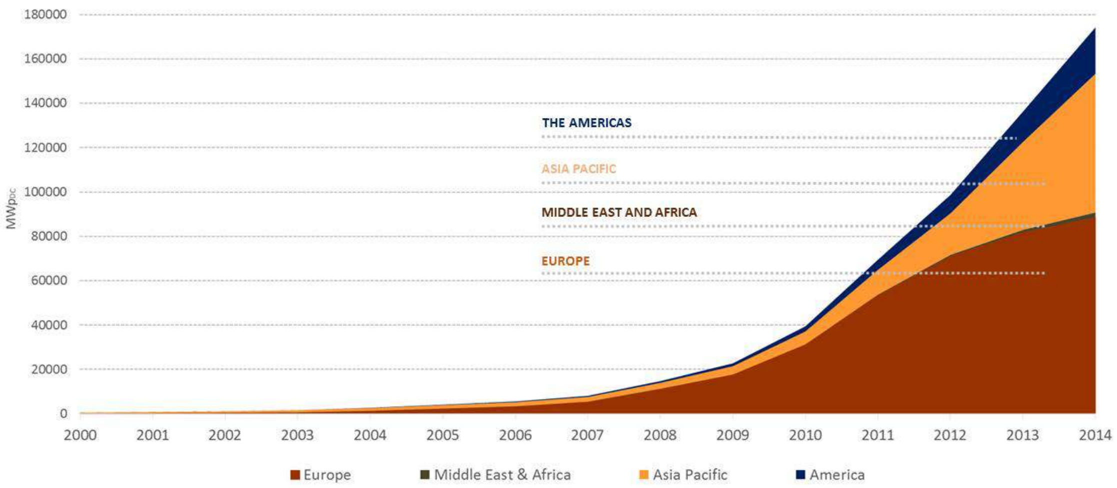

Figure 1.1: Evolution of regional PV installations [3].

The high penetration of PV systems has consequences. One of the problems is the variability associated with PV energy generation. PV power output depends essentially on the irradiance incident on the panels, which can change very fast due to moving clouds. The network and all the other generation sources must be prepared to accommodate this variability. Variability prediction methods can prove a useful tool both in network planning and in future PV sites selection.

2. Characterization of variable PV generation

Solar photovoltaic (PV) systems power output depends essentially on the global irradiance to which they are subjected. Therefore, it is necessary to understand irradiance variability and its consequences. Changes in solar irradiance that affect PV systems occur in a wide range of timescales, from few milliseconds to several decades. Each of these changes will cause a different kind of impact on the power system (Table 2.1).

Table 2.1: Potential power system impacts of solar irradiance variability

Timescale of changes in solar irradiance	Potential power system impact
Seconds	Power quality (e.g. voltage flicker)
Minutes	Regulation reserves
Minutes to hours	Load following
Hours to days	Unit commitment
Months to years	Missing storage and/or capacity

The sun is a variable star at all observed timescales and at all wavelengths. However the sun's variability of the time range between seconds and hours are by far lower than the one induced by clouds (Fig. 2.1).

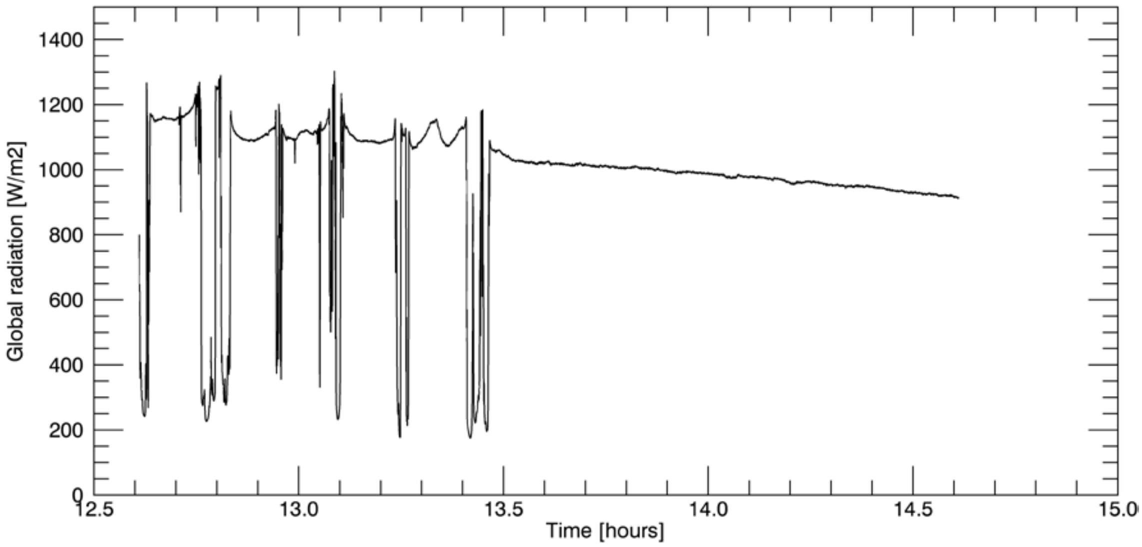

Figure 2.1: Global radiation measured at Oahu (see chapter 4.1.1 [4]) on March 30th, 2010 in one second time resolution. Until 13:30 effects of clouds are clearly visible (strong dips and ridges). After 13:30 the radiation is lowering slightly due to the sun's trajectory, but is otherwise almost stable.

Solar variations in millisecond ranges are only scarcely investigated but can be assumed as small for global radiation and PV production. The influence of the sun's orbit is strong, but precisely predictable and therefore not handled here. Strong and regionally highly correlated gradients are induced by solar eclipses as seen in Europe in March 2015 [5]. Those are however seldom events – the next one in Central Europe with a noticeable effect will be in 2048 – and can be calculated well in advance and are therefore also not covered in this report.

In this work we will focus on the time range from seconds to several hours and the variability induced by the movement of clouds.

2.1. Impact of solar variability on the power system

The high variability of solar irradiance is a source of new challenges to the distribution system operators (DSO) and transmission system operators (TSO) concerning planning and unit commitment. Existing conventional generators will need to adapt to PV generation profiles in order to counteract introduced variability, and more flexible power plants, particularly in response time, may have to be included in the available generation mix. Other solutions, like demand side management and energy storage, may also be considered.

Changes in solar irradiance over short timescales may introduce a flicker in voltage, which can be harmful for consumers' equipment. Furthermore, if these changes have a large magnitude, generators responsible for mitigating that occurrence must be capable of changing their output quickly and with large magnitudes (large ramp rates), so proper load following can be carried out. Technical flexibility for conventional power generators are shown in Table 2.1.

Table 2.2: Flexibility of conventional power generation technologies (Source: IEA, 2014 [6])

Technology	Nuclear	Hard coal	Lignite	Combined Cycle Gas	Pumped Storage
Start-up time "cold"	48h	~0.6 - 8h	~0.6-6h	1-4h	~0.1h
Ramp rate	0.3-5%/min	0.6-8%/min	~0.6-6%/min	~0.8-15%/min	>40%/min
Minimal possible load	40-100%	20-60%	40-60%	15-50%	5-15%

Observations of point sensors show large changes in solar irradiance in just a few seconds. In [7], using six San Diego solar resource stations over a year, five 1-sec ramps up and 17 1-sec ramps down with magnitudes greater than 50% were detected, with a maximum change of 60% over 1-sec. However, as we will analyze further, it is more appropriate to consider area variability over point variability.

High penetration of PV systems may also lead to an increase in operating reserves since the system must be prepared for any sudden loss of generation and unexpected load fluctuations. This scenario implies an obvious increase in system costs. When increasing (decreasing) PV generation does not coincide with increasing (decreasing) load, a substantially larger response of standby generators will be required. The critical situation corresponds to an increase in load with a simultaneous decrease in PV generation, which typically happens when the sun is setting (however the effects of the sun path can be forecasted very well). Controlling PV systems output and energy storage can also be considered as solutions to tackle these issues.

2.2. Geographic dispersion and “smoothing effect”

Solar variability impacts in PV generation are different if a set of geographically dispersed systems is considered, instead of a single system. Several studies have been done on this subject and they all come to the conclusion that there is a strong reduction in variability when the aggregate of several PV systems is taken into account, rather than just one PV system. That is called the “smoothing effect”. This effect is mainly induced by the typical scales of clouds (1 – 10 km) and cloud speed and the scale of low and high pressure systems (1000 km).

Variability reduction (VR) is defined as the ratio of variance in a time-varying quantity at one site to the variance of the average of all sites in a network.

$$\mathrm{VR} = \frac{\sigma_{\Delta t}^{1}}{\sigma_{\Delta t}^{Fleet}} \tag{2.1}$$

In 2008, Curtright and Apt [8] investigated real power output data with 10 minute resolution from three sites hundreds of kilometers apart: a 228.5 kW system in Prescott, Arizona, a 144 kW system in Scottsdale, Arizona, and a 121 kW system in Yuma, Arizona. Approximately one month of consecutive data (June 22 – July 27, 2006) was analyzed and VR values of 1.7 to 3.3 for 10-min steps of power output were found. In 2010, a similar study was carried out by Lave and Kleissl [9]. Analyzing a year (January 1 – December 31, 2008) of 5 minute radiation data from four sites hundreds of kilometers apart in Colorado, VR values of 2.4 to 4.1 were found. These studies, among others, confirm that the variability associated with a fleet of PV systems is significantly lower than the variability associated with a single PV system.

In the special case when the change in output between locations is uncorrelated, fleet capacity is equally distributed and the variance at each location is the same, Hoff and Perez (2010) showed that fleet output variability equals the output variability at a single location divided by the square root of the number of locations [10]:

$$\sigma_{\Delta t}^{\mathrm{Fleet}} = \frac{\sigma_{\Delta t}^{1}}{\sqrt{\mathrm{N}}} \tag{2.2}$$

A similar result was derived by Kato *et al.* (2011) [11] that relates variability to the square root of the number of systems when the locations are uncorrelated. The correlation coefficient decreases as the distance between sites increases and increases as the timescale of changes increases, as demonstrated by Mills and Wiser (2010) [12].

Table 2.3: Relation between correlation, distance between sites and timescale of changes.

	Correlation
Distance between sites ↗	↘
Timescale of changes ↗	↗

This means that changes in output in two different locations are more correlated if the distance between those locations becomes smaller. Thus, it is important to study methods that, in a project scenario, can help estimate the power output variability of a group of PV systems at a given location, whether it is a centrally located plant or a group of small distributed systems. Ignoring the smoothing effect when calculating energy storage requirements will result in overestimation of the reserves, and consequently in extra costs [13].

3. PV variability models

Increased use of PV systems has raised questions about potential impacts of variable generation, as explained in Chapter 2. Having in mind a future scenario with high penetration of PV systems, it is necessary to explore methods that quantify such variability in order to study new possible locations for PV systems as well as possible energy storage requirements. Since the most potentially harmful variations are those which occur within a short interval of time, due to its rapid change in net load, these methods must be able to estimate changes in power output in such timescales with high reliability, in order to establish guidelines that allow the mitigation of such problems. Also, the plant spatial distribution must be taken into account in order to simulate the regional smoothing effect.

This section gives an overview over existing methods for estimation of variability in PV systems, advantages and disadvantages, and a final decision on what methods are best suited for this activity's needs. Those methods will be explained in more detail.

3.1. Existing methods to describe variability

3.1.1. Method 1: Representative Blocks

The first method presented here was developed by Kato *et al.* (2011) [11]. This method aims to estimate the standard deviation of total power output fluctuation of high penetration photovoltaic power generation system dispersed over a large area.

The proposed method assumes that the area to be studied consists of a number of subgroups and each subgroup consists of N blocks, each with an installed PV capacity P_n, standard deviation of insolation fluctuation σ_n, and performance ratio η. The distance between center points of two neighboring blocks is d. This is the most important value in the proposed method, because insolation patterns at two points must be considered as independent. Figure 3.1 summarizes this description.

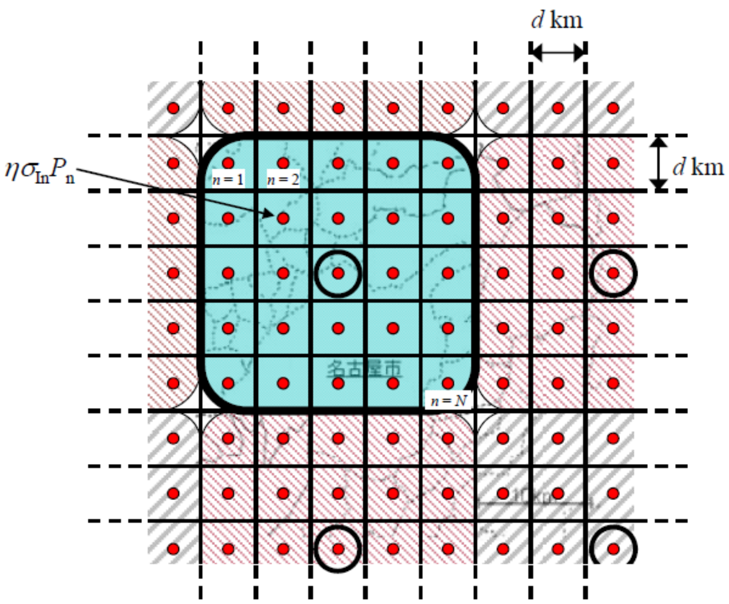

Figure 3.1: Modeling of area by a number of subgroup consisting of N blocks of d x d. [11]

The probabilistic characteristic of insolation fluctuation is assumed to be the same for all N blocks. Also, the PV capacity is assumed to be equally distributed. The performance ratio can be considered constant. As mentioned before, the fleet output variability calculated by this method is given by equation (2.2).

3.1.2. Method 2: Dispersion Factor Method and ramp rate correlation

Method 2 was proposed by Hoff and Perez (2010) [10]. The objective of this method is to provide a general model that quantifies the short-term power output variability resulting from an ensemble of arbitrarily configured PV systems. The output variability is defined as a measure of the PV fleet's power output changes over a selected sampling time interval and analysis period relative to PV fleet capacity:

$$\sigma_{\Delta t}^{\text{Fleet}} = \frac{1}{C^{\text{Fleet}}} \sqrt{Var\left[\sum_{n=1}^{N} \Delta \boldsymbol{P}_{\Delta t}^{\boldsymbol{n}}\right]} \tag{3.1}$$

where C^{Fleet} is the total installed peak power of the fleet and $\Delta \boldsymbol{P}_{\Delta t}^{\boldsymbol{n}}$ is a random variable that represents the time-series of changes in power at the n$^{\text{th}}$ PV installation using a sampling time interval of Δt defined over an analysis period. $\Delta \boldsymbol{P}_{\Delta t}^{\boldsymbol{n}}$ corresponds also to the temporal ramp rate which can be used as general variability measure. It can also be adopted for time series of clear-sky index instead of PV production (see Eq. 3.16).

A Dispersion Factor (D) is introduced representing the relationship between PV fleet configuration, cloud transit speed and a defined time interval:

$$D = \frac{L}{V\Delta t} \tag{3.2}$$

where L is the length of the considered PV fleet in the direction of cloud motion and V is the transit rate. The PV fleet considered in the study is a 1-dimensional set of N identical, equally-spaced, installations. The Dispersion Factor increases as the cloud speed decreases and/or as the distance between installations increases.

Figure 3.2 illustrates the Dispersion Factor for three cases: a fast, medium, and slow cloud transit speed across a PV fleet with 4 PV systems. The fast-moving cloud in the top section of the figure crosses the PV fleet in $2\Delta t$, and thus D equals 2. The medium transit speed requires $4\Delta t$ for a cloud to cross the PV fleet, and therefore D equals 4. The slow transit speed in the bottom would result in a Dispersion Factor of 8.

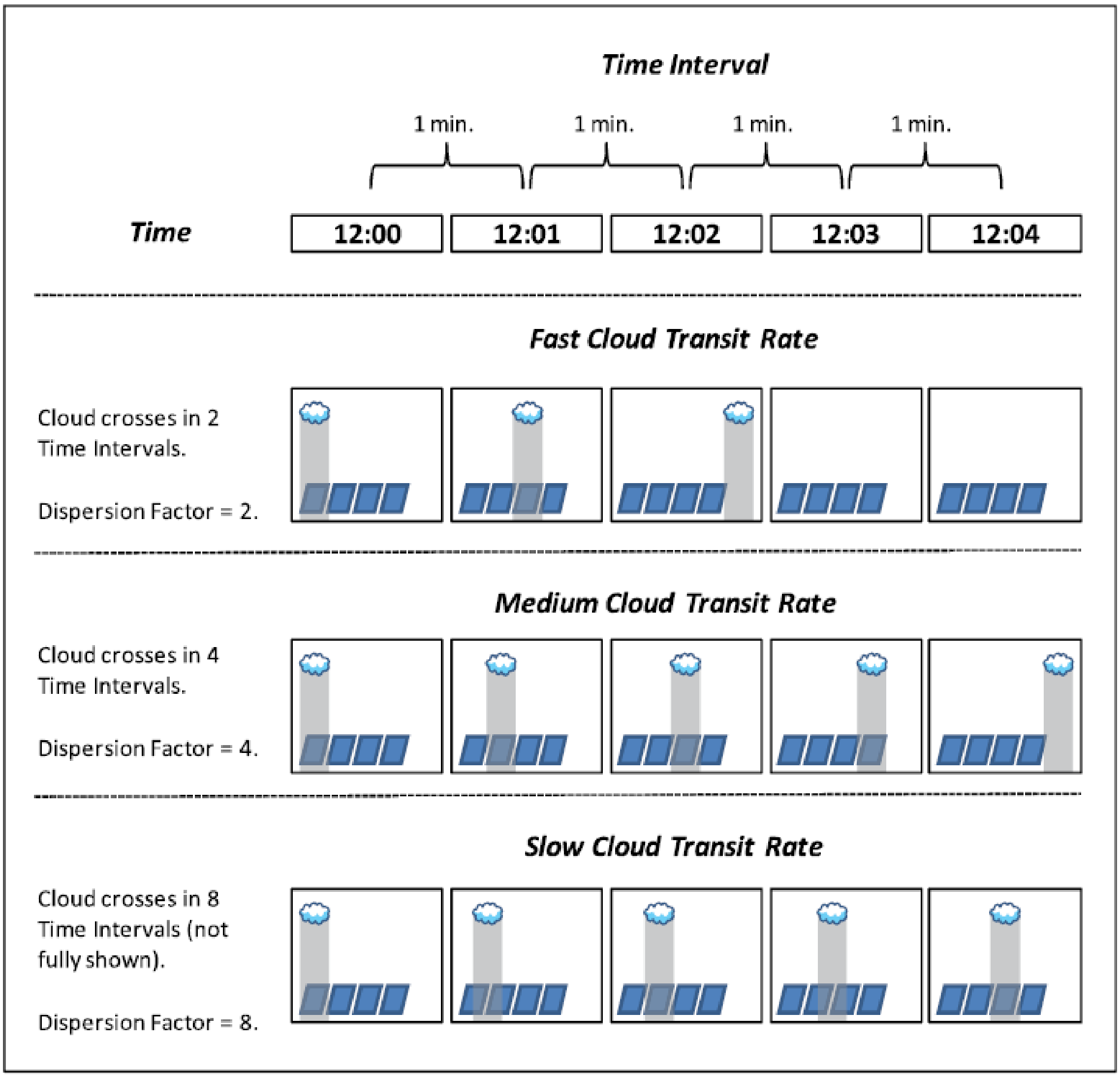

Figure 3.2: Dispersion Factor for a PV fleet with 4 PV systems using a 1-minute time interval when the cloud transit rate is fast, medium, or slow. [10]

The model establishes four different Dispersion Factor regions, each with a different expression for the output variability (ratio of the output variability for the PV fleet to output variability of the same PV fleet concentrated in one single location):

Crowded region: The number of PV systems in the fleet is greater than the Dispersion Factor (N>D). As depicted in the top section of Figure 3.2, a cloud disturbance affects more than one PV system in one time interval. In this case, output variability may be expressed as:

$$\sigma_{\Delta t}^{fleet} = \frac{\sigma_{D\Delta t}^{local}}{D} \tag{3.3}$$

Relating to a centralized PV plant, which can be considered a crowded region, this model suggests that output variability, in this case, is independent of the number of systems.

Optimal point: The number of PV systems in the fleet equals the Dispersion Factor. In this case (middle section of Figure 3.2), a cloud disturbance will affect each system for exactly one time interval. For this case, equation (3.1) assumes the following solution:

$$\sigma_{\Delta t}^{fleet} = \frac{\sigma_{N\Delta t}^{local}}{N} \tag{3.4}$$

Limited region: The number of PV systems is smaller than the Dispersion Factor. Illustrated in the bottom section of Figure 3.2, a cloud disturbance will affect each system longer than one time interval. In this case, although equation (3.1) cannot be solved for a specific solution, it is possible to define an upper bound for the variability:

$$\sigma_{\Delta t}^{fleet} < \frac{\sigma_{\Delta t}^{local}}{\sqrt{N}} \tag{3.5}$$

Spacious region: The number of PV systems is much smaller than the Dispersion Factor. In this situation, short-term fluctuations of each PV system are independent of each other. Solving equation (3.1) will lead us to equation (2.2).

Combining equations (2.2), (3.3), (3.4) and (3.5), the relative output variability for N PV systems leads to the following diagram:

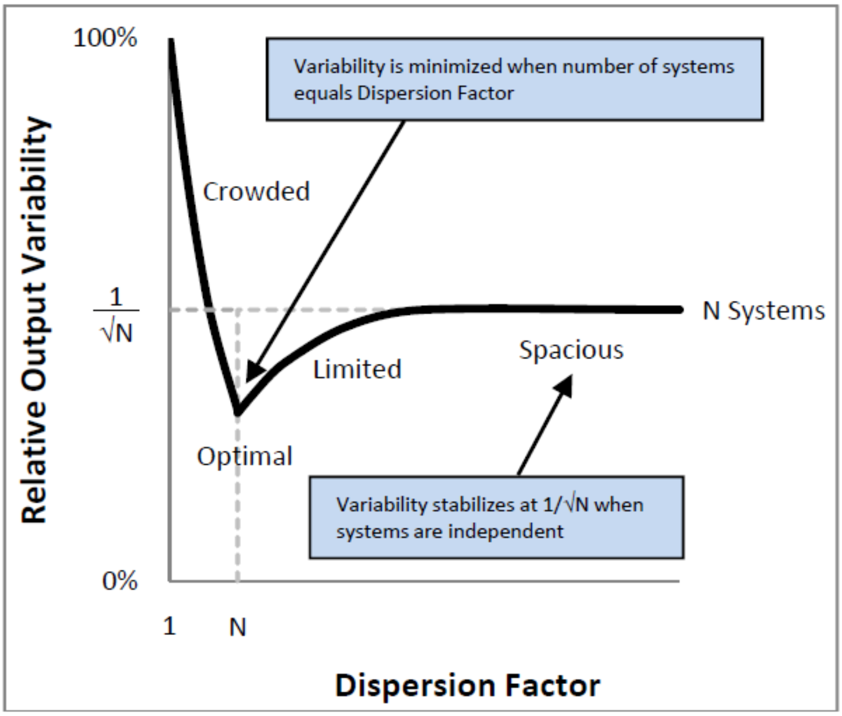

Figure 3.3: Relative output variability as a function of the Dispersion Factor for a fleet of N PV systems. [9]

This method suggests that there is an optimal point, as discussed before, where the output variability of the PV fleet equals $\frac{1}{N}$ times that of a single system using a time interval of $N\Delta t$, from equation (3.4).

Further work was undertaken by the same authors in [1], where a different approach is adopted. Taking equation (3.1) one can derive the following equation:

$$\sigma_{\Delta t}^{\text{Fleet}} = \frac{1}{C^{Fleet}} \sqrt{\sum_{i=1}^{N} \sum_{j=1}^{N} \sigma_{\Delta t}^{i} \sigma_{\Delta t}^{j} \rho_{\Delta t}^{i,j}} \tag{3.6}$$

from which one may conclude that the (normalized) output variation of the fleet is dependent on the output variation of each location and the correlation between them. Empirical data revealed that a model for the correlation between sites, based on equation (3.7) fitted well, as long as using location-specific parameters:

$$\rho = \frac{1}{1 + \frac{d}{(\Delta t)(CS_1)}} \tag{3.7}$$

where the term d refers to distance (km) and CS_1 refers to cloud speed (km/h) in a specific site (distances in m and cloud speed in m/s are also viable).

Optionally another fitting equation presented by Perez (2014) [13] will be used in the following case studies:

$$\rho = e^{\frac{d \ln(0.2)}{1.5\,(\Delta t)(CS_2)}} \tag{3.8}$$

where CS_2 refers to the cloud speed (km/h).

3.1.3. Method 3 (Wavelet analysis)

Another method discussed here is the one developed by Lave *et al.* (2011) [15] [16]. This method proposes a Wavelet Variability Model (WVM) for simulating power plant output, given 1) measurements from a single irradiance point sensor, 2) knowledge of the power plant footprint (the location of each PV panel) and PV capacity, and 3) a correlation scaling coefficient, by determining the geographic smoothing that will occur over the area of the plant. The simulated system may be centrally located or distributed generation.

First, correlations between sites within the power system are determined using an equation based on the distance between sites ($d_{m,n}$), timescales ($\bar{t}$), and a correlation scaling coefficient (A value):

$$\rho(d_{m,n}, \bar{t}) = \exp\left(-\frac{1}{A}\frac{d_{m,n}}{\bar{t}}\right) \tag{3.9}$$

The A value can be found using a small network of irradiance sensors (at least $\sim$ 4-6 sites) where the correlations, distances, and timescales are known and equation (3.6) may be solved for. The A value varies day-by-day and by location due to changing cloud speed. Smaller A values (1-3, typically observed at coastal sites with low, slow clouds) result in lower correlations between sites, while large A values ($>$ 4, typical of inland sites with high, fast-moving clouds) mean higher correlations.

An alternative way of computing the A value is proposed by the same authors in [17], in case a network of irradiance sensors is not available. The authors investigated the dependence of the A value on cloud speed and cloud size by using a simple cloud simulator. A values were found to increase both with increasing wind speed and with increasing cloud size. However, it was found that the impact of cloud size was small, and that A values were nearly linearly proportional to cloud speed. The following equation was found to adequately represent the A value, based on cloud speed (cs) [m/s]:

$$A = 0.5 \times cs \tag{3.10}$$

From the correlations, VR, or the ratio of variability of a single point sensor to the variability of the entire PV plant, at each fluctuation timescale is found:

$$\mathrm{VR}(\bar{t}) = \frac{N^2}{\sum_{m=1}^{N}\sum_{n=1}^{N}\rho\left(d_{m,n},\bar{t}\right)} \qquad (3.11)$$

where N is the total number of sites. A single site is chosen to be an area over which $\rho\left(d_{m,n},\bar{t}\right) \approx 1$ for the timescales of interest. For distributed plants, a single site is one rooftop PV system. For utility-scale plants, a single site is a small container of PV modules, as dictated by computational limitations. Defined this way, $\mathrm{VR} = N$ for entirely independent sites ($\rho = 0, m \neq n$), and $\mathrm{VR} = 1$ for entirely dependent sites.

Wavelet decomposition is then used to separate the normalized input point sensor time-series by fluctuation timescale. By combining the wavelet modes at each timescale with the VR at each timescale, the normalized plant average irradiance is simulated. Simulated power output (in MW) is then obtained by using a clear-sky model for power output.

The time-series of fluctuations of actual power plant output and simulated power plant output are not expected to match perfectly, since only a single point sensor is used as input, but the statistics of the fluctuations are expected to agree.

3.2. Further temporal variability measures

In the literature further measures of variability and stability can be found. In order to give a complete overview those are presented here. However they will not be used in the following case studies.

Perez et al. [18] introduced a stability index for his global to diffuse model:

$$\rho = (|k_t' - k_{t-1}'| + |k_t' - k_{t+1}'|)/2 \qquad (3.12)$$

where k'_t is an air mass corrected clearness index:

$$k_t' = k_t/\{1.031 \cdot exp[-1.4/(0.9 + 9.4/m)] + 0.1\} \qquad (3.13)$$

and m refers to the optical air mass (see 3.27) and k_t to the clearness index (see 3.49).

A similar variability index used Skartveit and Olseth [19] in their global to diffuse model:

$$\rho = \{[(k_t - k_{t-1})^2 + (k_t - k_{t+1})^2]/2\}^{0.5} \qquad (3.14)$$

Stein et al. proposed [20] another Variability Index (VI):

$$VI = \frac{\sum_{k=2}^{n}\sqrt{(GHI_k - GHI_{k-1})^2 + \Delta t^2}}{\sum_{k=2}^{n}\sqrt{\left(GHI_{cs,k} - GHI_{cs,k-1}\right)^2 + \Delta t^2}} \qquad (3.15)$$

3.3. Chosen models

The main focus of the first method is the magnitude of changes in global horizontal insolation, and not so much the timescale in which they occur, which is contrary to the purposes of the present study. For the method to produce realistic results different representative points over the area of interest must be selected and solar data must be available for those points. Otherwise, large values of the standard deviation would be overestimated and small values would be underestimated.

The Dispersion Factor method requires irradiance readings from all the systems in the PV fleet, i.e. many different locations, which is sometimes difficult or even impossible to obtain. In alternative we can use the local variability and correlation between sites, which can be a more practical approach if the number of sites isn't too large.

The wavelet analysis has the advantage of being able to study the variability of a set of PV systems over any desirable timescale, provided that the irradiance data has proper resolution. Furthermore, it only needs solar irradiance data from a single sensor (this may change if correlation scaling factor A is unknown; still only a small network of 4-6 sensors would be required), unlike the previous methods, significantly reducing the data requirements.

The three methods performed well in terms of model validation carried out by the authors, with no real distinction between them. However, for the reasons discussed above, the two selected methods to be studied in a deeper manner and tested with real data were the Dispersion Factor and the Wavelet Variability Model. The following sections will explore the method in greater detail, namely the required data inputs, the appropriate time resolution for the data collection and the explanation of the algorithm.

3.3.1. Required data input

The Wavelet Variability Model will require the following data inputs:

- Global Horizontal Irradiance (GHI) time-series from a single point sensor;
- Altitude;
- Latitude;
- Longitude;
- Day of year (DoY);
- Local Standard Time Meridian (LSTM);
- Local Time;
- PV footprint;
- PV capacity;
- PV tilt;
- PV azimuth;
- Correlation scaling factor A.

3.3.2. Relevant time resolution of data collection

The fluctuations that will likely be more attenuated when going from a single PV system to a group of systems are those that occur in short timescales (seconds). For this reason, it is important that the available dataset has a high enough resolution, so those fluctuations can be taken into account by the method.

The ideal resolution would be one reading per second, as it would bring insight on most of the potential impacts the power systems is subjected to. However, this could be extremely demanding for data storage capacity. If this becomes a problem, it is necessary to find a reasonable value for the time resolution of data collection. Woyte et al. (2001) [21] conducted a study over three months, with data resolution of one reading per second, and concluded that only 1% to 2% of the fluctuations occur in timescales shorter than 5 seconds. Therefore, a dataset with one reading per 5 seconds would be less severe for data storage requirements while preserving great part of the information, being an appropriate choice for the time resolution of data collection.

3.3.3. Algorithm explanation

The starting point of this algorithm is the global horizontal irradiance (GHI) time series of a single point sensor. To obtain a stationary signal, the irradiance time series is normalized so that output during clear-sky (cs) conditions is 1:

$$\mathrm{k}_c(t) = \frac{\mathrm{GHI}(t)}{\mathrm{GHI}_{\mathrm{cs}}(t)} \tag{3.16}$$

where $\mathrm{k_c}(t)$ is the clear-sky index and $\mathrm{GHI_{cs}}(t)$ is the clear-sky model. By obtaining the clear-sky index, we eliminate the changes caused by the natural course of the day (to correct the influence of the solar elevation angle). In this method, the authors assumed a statistically invariant irradiance field both spatially and in time over the day (i.e. stationary), and that correlations between sites are isotropic: they depend only on distance, not direction. The Solis model [22] was used as clear-sky model.

One of the parameters used in the Solis model is the solar elevation angle, thus solar geometry calculations are required first. To calculate the solar elevation angle, we will need 1) the declination angle, and 2) the hour angle.

Declination angle

The declination of the sun (δ) is the angle between the equator and a line drawn from the center of the Earth to the center of the sun. This angle varies seasonally due to the tilt of the Earth on its axis of rotation and the rotation of the Earth around the sun. The declination angle (in degrees) is calculated using the following equations:

$$\delta = \sin^{-1} 0.3978 \sin(b_1 - 1.4 + 0.0355 \sin(b_1 - 0.0489)) \tag{3.17}$$

$$b_1 = \frac{2\pi}{365.25} \times DoY \tag{3.18}$$

where DoY is the day of year, with January 1st being day 1.

Hour angle

The hour angle (ω) converts the Local Solar Time into the number of degrees which the sun moves across the sky. By definition, the hour angle is 0 ° at solar noon. The first thing we need to compute the hour angle is the equation of time (EoT):

$$EoT[\mathrm{h}] = -0.128\sin(b_2 - 2.8) - 0.165\sin(2b_2 + 19.7) \tag{3.19}$$

$$b_2 = \frac{360}{365.25} \times DoY \tag{3.20}$$

The equation of time is an empirical equation that corrects for the eccentricity of the Earth's orbit and the Earth's axial tilt. The Local Solar Time (LST) can be found by using the following equations:

$$LST = LT + \frac{(longitude - LSTM)}{15} + EoT \tag{3.21}$$

$$LSTM = 15 \times \Delta T_{GMT} \tag{3.22}$$

where LT is the Local Time in hours, $LSTM$ is the Local Standard Time Meridian in degrees and ΔT_{GMT} is the difference of the Local Time from Greenwich Mean Time in hours.

Finally, the hour angle (in degrees) is given by equation (3.23):

$$\omega = 15 \times (LST[\mathrm{h}] - 12) \tag{3.23}$$

Elevation and azimuth angles

The elevation angle (h_s) is the angular height of the sun in the sky measured from the horizontal. The elevation angle varies through the day. It also depends on the latitude of a particular location and the day of the year. The elevation angle can be found using the following formula:

$$h_s = \sin^{-1}(\cos\phi\cos\delta\cos\omega + \sin\phi\sin\delta) \tag{3.24}$$

where ϕ is the latitude of the site. The solar azimuth angle (α_s) – the horizontal angle between the vertical plane containing the center of the solar disc and the vertical plane running in a true north-south direction – is obtained from:

$$\cos\alpha_s = \frac{\sin\phi\sin h - \sin\delta}{\cos\phi\cos h_s} \tag{3.25}$$

$$\sin\alpha_s = \frac{\cos\delta\sin\omega}{\cos h_s} \tag{3.26}$$

If $\sin\alpha_s < 0$ then $\alpha_s = -\cos^{-1}(\cos\alpha_s)$; if $\sin\alpha_s > 0$ then $\alpha_s = \cos^{-1}(\cos\alpha_s)$

Solis Model

Ineichen [22] proposed a simplified version of the Solis clear-sky model for horizontal global irradiance. The basis of the model is the Lambert-Beer relation, which expresses the normal beam irradiance reaching the ground (I_{nb}) as a function of extraterrestrial irradiance (I_0), the aerosol optical depth (τ) and the optical air mass (m):

$$\mathrm{I_{nb}} = \mathrm{I_0} \cdot \mathrm{e}^{(-\mathrm{m}\cdot\tau)} \tag{3.27}$$

Modifying expression (3.27), due to the non-linear nature of the exponential function, and subsequently adapting it to global horizontal irradiance (Mueller, 2004) [23], one obtains the following equation:

$$GHI_{cs} = I_0 \cdot e^{\left(-\frac{\tau}{\sin^{\mathrm{g}} h}\right)} \cdot \sin h_s \tag{3.28}$$

where h_s is the sun's elevation angle and g is the fitting parameter obtained from RTM calculations at two different solar elevation angles.

For areas with high values of aerosol content, it is necessary to use a modified extraterrestrial irradiance and expression (3.28) assumes the following form:

$$GHI_{cs} = I'_0 \cdot e^{\left(-\frac{\tau_{\mathrm{g}}}{\sin^{\mathrm{g}} h}\right)} \cdot \sin h_s \tag{3.29}$$

where I_0' is the enhanced extraterrestrial irradiance, τ_{g} the global optical depth, and g the fitting parameter obtained from RTM calculations.

$$I_0' = I_0 \cdot [I_{0,2} \cdot \tau_{700}^2 + I_{0,1} \cdot \tau_{700} + I_{0,0} + 0.071 \cdot \ln(\frac{p}{p_0})] \tag{3.30}$$

with

$$I_{0,0} = 1.08 \cdot w^{0.0051} \tag{3.31}$$

$$I_{0,1} = 0.97 \cdot w^{0.032} \tag{3.32}$$

$$I_{0,2} = 0.12 \cdot w^{0.56} \tag{3.33}$$

$$I_0 = 1366 \cdot \left(1 + 0.033 \cdot \cos\left(\frac{2\pi}{365.25} \cdot DoY\right)\right) \tag{3.34}$$

and p is the atmospheric pressure at the desired location, p_0 the atmospheric pressure at sea level and w the water vapor column. Index 700 refers to the wavelength at which the aerosol optical depth is taken, which is 700 nm, due to the broadband and monochromatic equivalence of the aerosol optical depth at this wavelength.

Coefficients for equation (3.29) are the following:

$$\mathrm{\tau_g = t_{g,1} * \tau_{700} + t_{g,0} + t_{g,p} * \ln(\frac{p}{p_0})} \tag{3.35}$$

$$t_{g,1} = 1.24 + 0.047 * \ln(w) + 0.0061 * ln^2(w) \tag{3.36}$$

$$t_{g,0} = 0.27 + 0.043 * \ln(w) + 0.0090 * ln^2(w) \tag{3.37}$$

$$\mathrm{t_{g,p} = 0.0079 * w + 0.1} \tag{3.38}$$

and

$$g = -0.0147 * \ln(w) - 0.3079 * \tau_{700}^2 + 0.2846 * \tau_{700} + 0.3798 \tag{3.39}$$

Values for the aerosol optical depth at 550 nm and water vapor column were taken from available public access datasets from NASA's Giovanni data portal (http://disc.sci.gsfc.nasa.gov/giovanni) for the wavelet model and from http://www.gmes-atmosphere.eu/ for the Dispersion Factor Model. Values for the Angstrom exponent (α) were also obtained to convert optical depth (τ_λ) to the relevant wavelength, using the following relation:

$$\tau_\lambda = \tau_{\lambda_0}(\frac{\lambda}{\lambda_0})^{-\alpha} \tag{3.40}$$

Atmospheric pressure was calculated with the following formula using the following relation:

$$p = p_0 * (1 - \frac{L * h}{T_0})^{\frac{g*M}{R*L}} \tag{3.41}$$

where T_0 is the sea level temperature, g is the gravitational acceleration, L is temperature decrease rate, R is universal gas constant, M the molar mass of dry air and h is the sites altitude.

Wavelet transform

The next step is the application of the wavelet transform to the clear-sky index $\mathrm{k_t}(t)$:

$$w_{\bar{t}}(t) = \int_{t_{\text{start}}}^{t_{\text{end}}} \mathrm{k_t}(t') \frac{1}{\sqrt{\bar{t}}} \psi\left(\frac{t'-t}{\bar{t}}\right) dt' \tag{3.42}$$

where $\bar{t}$ is the wavelet timescale (duration of fluctuations) and t_{start} and t_{end} are the beginning and the end of the GHI time-series. The Haar wavelet was chosen as a basis function ($\psi(T)$) due to its simplicity and similarity with the bi-modal steps in clear-sky index. The Haar wavelet is defined by:

$$\psi(T) = \begin{cases} 1, & 0 \le T < 1/2 \\ -1, & 1/2 \le T < 1 \\ 0, & \text{otherwise} \end{cases} \tag{3.43}$$

The wavelet modes are denoted by $w_{\bar{t}}(t)$, where $\bar{t}$ is increased by factors of 2, i.e. $\bar{t} = 2^j$.

Correlations

The correlations between “sites” within the PV system ($\rho(d_{m,n}, \bar{t})$), as proposed by Lave *et al.* [15], is given by:

$$\rho(d_{m,n}, \bar{t}) = \exp\left(-\frac{1}{A}\frac{d_{m,n}}{\bar{t}}\right) \tag{3.44}$$

where $d_{m,n}$ is the distance between sites m and n, $\bar{t}$ is the timescale of fluctuations and A is the correlation scaling factor. The A value can be found using a small network of 4-6 irradiance sensors where correlations and distances are known. Using these values, equation (3.44) may be solved for A. Another way of computing A is using equation (3.10) and the wind speed (at cloud altitude).

Variability reduction

The variability reduction ($\mathrm{VR}(\bar{t})$), for each timescale, is the ratio between the variance of the point sensor and the variance of the entire PV system, and is defined by:

$$\mathrm{VR}(\bar{t}) = \frac{N^2}{\sum_{m=1}^{N}\sum_{n=1}^{N}\rho(d_{m,n}, \bar{t})} \tag{3.45}$$

where N is the total number of sites. Defined this way, $\mathrm{VR} = N$ for entirely independent sites ($\rho = 0, m \neq n$), and $\mathrm{VR} = 1$ for entirely dependent sites.

Simulated wavelet modes of PV system

The wavelet modes of the simulated PV system are obtained using $\mathrm{VR}(\bar{t})$ and equation (3.46):

$$w_{\bar{t}}^{\mathrm{sim}}(t) = \frac{w_{\bar{t}}(t)}{\sqrt{\mathrm{VR}(\bar{t})}} \tag{3.46}$$

Then, these wavelet modes can be compared to the wavelet modes of the actual power output of the PV system, to test the accuracy of the model.

Wavelet modes of the actual power output of PV system

To obtain the wavelet modes of the actual power output of the PV system a clear-sky power output model is needed. This model ($P_{\mathrm{cs}}(t)$) is created by combining a plane of array irradiance clear-sky model ($POI_{\mathrm{cs}}(t)$) with the system's capacity (SC) and a constant conversion factor (C):

$$P_{\mathrm{cs}}(t) = POI_{\mathrm{cs}}(t) \times SC \times C \tag{3.47}$$

The conversion factor is obtained by:

$$C = \frac{DF}{1000} \tag{3.48}$$

where DF is a derate factor that accounts for temperature, wiring, MPP and inverter losses. The clear-sky power model chosen here is simple, but in applications of the Wavelet Variability Model it could easily be replaced by a more accurate user-defined model. The Page model [24] was used as the plane of array irradiance clear-sky model (in chapter 4.2). Since this model requires diffuse irradiance as input, diffuse fraction was estimated according to Ridley *et al.* [25].

Diffuse fraction model

This model allows us to estimate the diffuse radiation from measurements of global radiation. The diffuse fraction is defined as the ratio between diffuse radiation (I_{diffuse}) and global radiation (I_{global}):

$$d_t = \frac{I_{\text{diffuse}}}{I_{\text{global}}} \tag{3.49}$$

RIdley et al. have demonstrated a statistically rigorous method of constructing a closed form function model for the diffuse fraction. The equation for the generic model of diffuse fraction is:

$$d_t = \frac{1}{1 + \mathrm{e}^{-5.38+6.63\times k_t+0.006\times LST-0.007\times h_s+1.75\times K_t+1.31\psi}} \tag{3.50}$$

where k_t is the clearness index, i.e. the ratio between global radiation and extraterrestrial radiation:

$$k_t = \frac{I_{\text{global}}}{I_0} \tag{3.51}$$

LST and h_s are Local Solar Time and solar elevation angle, respectively, which have already been defined. K_t is the daily clearness index:

$$K_t = \frac{\sum_{j=1}^{24} I_{\text{global}_j}}{\sum_{j=1}^{24} I_{0_j}} \tag{3.52}$$

similar to k_t but for hourly values.
And ψ which is given by the expression:

$$\psi(t) = \begin{cases} \dfrac{k_{t-1} + k_{t+1}}{2}, & sunrise < t < sunset \\ k_{t+1}, & sunrise \\ k_{t-1}, & \text{sunset} \end{cases} \tag{3.53}$$

Page model

The Page model provides the irradiance on inclined planes, using global and diffuse irradiance as inputs. If we use clear-sky global and diffuse irradiance as inputs, the result will be the clear-sky plane of array irradiance. Page model was selected due to its simplicity. Alternatively many other diffuse models like Perez et al. [26], which are more complex but show lower uncertainties, are available.

The plane of array irradiance ($G(\beta,\alpha)$) is divided into three components: beam ($B(\beta,\alpha)$), diffuse ($D(\beta,\alpha)$) and ground reflected ($R_g(\beta,\alpha)$). These components depend on the orientation (α) and tilt (β) of the irradiated plane. The total irradiance on an inclined plane is the sum of the three components:

$$G(\beta,\alpha) = B(\beta,\alpha) + D(\beta,\alpha) + R_g(\beta,\alpha) \tag{3.54}$$

Before computing each of these components, it is necessary to calculate the solar incidence angle ($\upsilon(\beta,\alpha)$). This is the angle between the normal to the plane, on which the sun is shining, and the line from the surface passing through the center of the solar disc. The angle is given by:

$$\upsilon(\beta,\alpha) = \cos^{-1}(\cos h_s \cos \alpha_F \sin \beta + \sin h_s \cos \beta) \tag{3.55}$$

$$\alpha_F = \alpha_s - \alpha \tag{3.56}$$

where h_s is the solar elevation angle, β is the tilt of the inclined plane, α_s is the solar azimuth angle and α is the orientation of the inclined plane. The solar azimuth and the orientation of the plane are measured from due south in the northern hemisphere, clockwise from the true north. In the southern hemisphere, they are measured from due north, anticlockwise from true south.

The beam irradiance is given by:

$$B(\beta,\alpha) = \frac{I_{\text{global}}(1-d_t)}{\sin h_s} \cos \upsilon(\beta,\alpha) \tag{3.57}$$

Before the computation of the diffuse component, a modulating function (K_b) is first calculated as:

$$K_b = \frac{I_{\text{global}}(1-d_t)}{\varepsilon \times 1366 \times \sin h_s} \tag{3.58}$$

$$\varepsilon = 1 + 0.03344 \cos\left(\frac{2\pi}{365.25} DoY - 0.048869\right) \tag{3.59}$$

where ε is the correction to mean solar distance on day DoY. K_b expresses the horizontal beam irradiance as a ratio to the extraterrestrial horizontal irradiance, corrected to mean solar distance. A diffuse function $f(\beta)$ is then calculated (β must be expressed in radians):

$$f(\beta) = \cos^2(\beta/2) + k[\sin \beta - \beta \cos \beta - \pi \sin^2(\beta/2)] \tag{3.60}$$

where k takes different values for northern Europe (k_N), considered represented by Bracknell, and southern Europe (k_S), considered represented by Geneva:

$$k_N = 0.00333 - 0.4150K_b - 0.6987K_b^2 \tag{3.61}$$

$$k_S = 0.00263 - 0.7120K_b - 0.6883K_b^2 \tag{3.62}$$

When $h > 5.7$ degrees, $D(\beta, \alpha)$ is found using the following formula:

$$D(\beta, \alpha) = d_t I_{\text{global}} \times \left(f(\beta)(1 - K_b) + K_b \frac{\cos \upsilon(\beta, \alpha)}{\sin h_s} \right) \tag{3.63}$$

When the solar elevation angle is below 5.7 degrees, the formula used to calculate $D(\beta, \alpha)$ is the following:

$$\begin{aligned} D(\beta, \alpha) = d_t I_{\text{global}} \times \cos^2(\beta/2)\,[1 + K_b \sin^3(\beta/2)] \\ \times [1 + K_b \cos^2 \upsilon(\beta, \alpha) \sin^3(90 - h_s)] \end{aligned} \tag{3.64}$$

The ground reflected irradiance is given by:

$$R_g(\beta, \alpha) = r_g \times \rho_g \times I_{\text{global}} \tag{3.65}$$

$$r_g = \frac{1 - \cos \beta}{2} \tag{3.66}$$

where r_g is the ground slope factor and ρ_g is the ground albedo.

4. Case studies

4.1. Dispersion Factor Model and ramp rate correlation

The Dispersion Factor Model (DFM) is demonstrated in six different regions (Table 4.1).

Table 4.1: Six different regions used for the Dispersion Factor Model

Region	Parameter	Period	Sites	Resolution	Approx. area
Oahu, Hawaii, USA	Radiation	6 days	17	1 sec.	1.0 km^2
Canton of Bern, CH	PV production	5 months	90	15 min.	10’000 km^2
Switzerland	Radiation	1 month	115	1 hour	50’000 km^2
United Kingdom	Radiation	12 months	18	1 hour	500’000 km^2
S. Great Planes, USA	Radiation	2 months	12	1 min.	50’000 km^2
Japan	Radiation	12 months	8	1 min.	500’000 km^2

We used both radiation and PV production data, assuming that the transformation between solar radiation and PV production is linear to a great extent (compared to the range of variability of the radiation).

The objective of this case study is to show the regional values of temporal and spatial variability and the parameters of the DFM model and to obtain a global model for the smoothing effects of distributed PV installations

The temporal variability has been studied additionally at 20 stations of the Baseline Surface Radiation Network (BSRN: http://www.bsrn.awi.de/).

4.1.1. Distributed generation – Oahu, Hawaii

The DFM was applied to a distributed system owned by the National Renewable Energy Laboratory (NREL), located in Oahu, Hawaii, USA. The system consists of a 17 global horizontal irradiance sensor grid (data available online [4]) spread across approximately 0.76 km^2, with 1 reading per second.

Figure 4.1: Sensor grid in Oahu, Hawaii, USA.

We analyzed 6 randomly chosen days for all seasons from May 2010 till March 2011 and time averages from 1 second to 3 minutes. Figure 4.2 shows the dependence of the correlation with distance between the locations for 1 second and 1 minute averages.

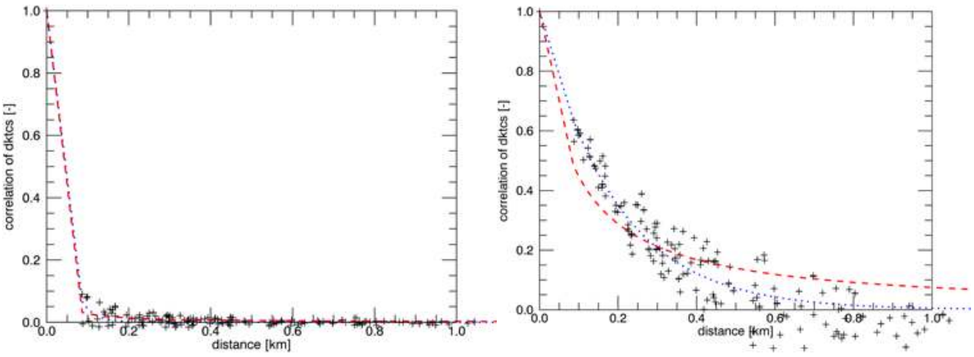

Figure 4.2: Correlation coefficients vs. distance for Oahu. Left: 1 second resolution, right: 1 minute resolution. Red line shows eq. 3.7, blue line eq. 3.8

The effect of time averaging is clearly visible. 1 second measurements show almost no correlation between two measurement sites, as the correlation is already low (<0.25) at less than 100 meters (the distances between the measurements locations are too big to evaluate this value). 1 minute averages show much higher correlation. The threshold for the correlation lower than 0.25 is reached at 265 m (exponential model). Table 4.2 gives an overview over all thresholds and model parameters. For NREL’s Oahu data the exponential model (Eq. 3.8) shows a better fit than using the hyperbolic model (Eq. 3.7).

Figure 4.3 shows the dependency of the threshold distance (spatial resolution) with a correlation of <0.25 on the time resolution.

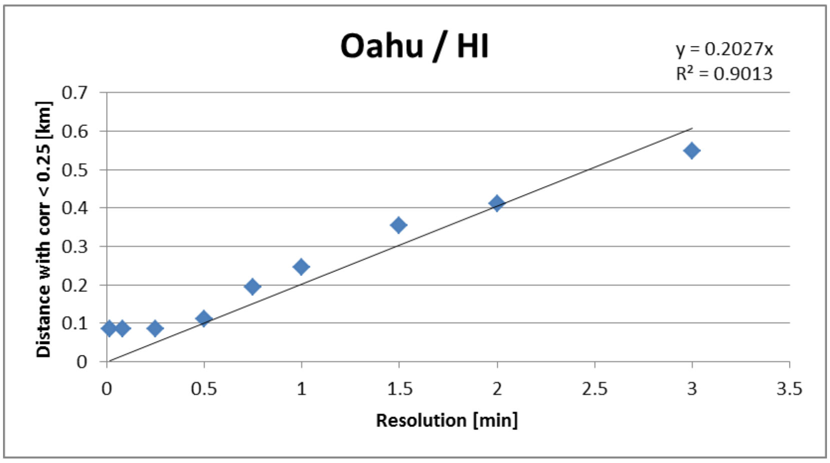

Figure 4.3: Distance with correlation < 0.25 vs. time resolution for Hawaii data (hyperbolic model).

The relationship is quite linear, although a slight lowering of the gradient at higher time resolutions is visible. The gradient is quite low, induced by relative low cloud speed (approximately 5 km/h). At very small time resolutions (1 sec.) the distances are too high, as the measurement stations are not dense enough (the nearest distances are 89 m).

4.1.2. Distributed generation – Canton of Bern

The DFM was applied to a network of 90 PV installations within the Canton of Bern with a total of capacity of 8 MW. The source of the data is Energiepool Switzerland, which handles the production of the installations with a fed-in-tariff with more than 30 kVA within Switzerland. The data are available in 15 minute resolution.

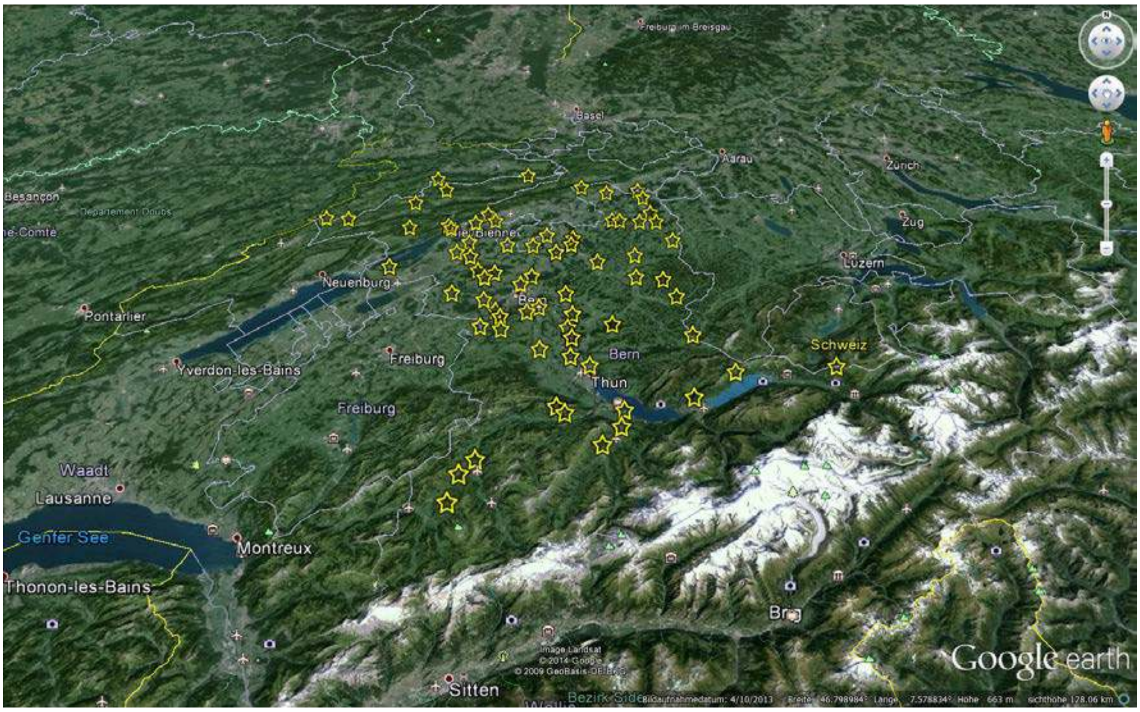

Figure 4.4: 90 PV installations with > 30 kVA, Canton of Bern.

We analyzed the period from June till November 2013 and the time averages from 15 to 90 minutes. In Figure 4.5 the spatial smoothing effect during three days is clearly visible

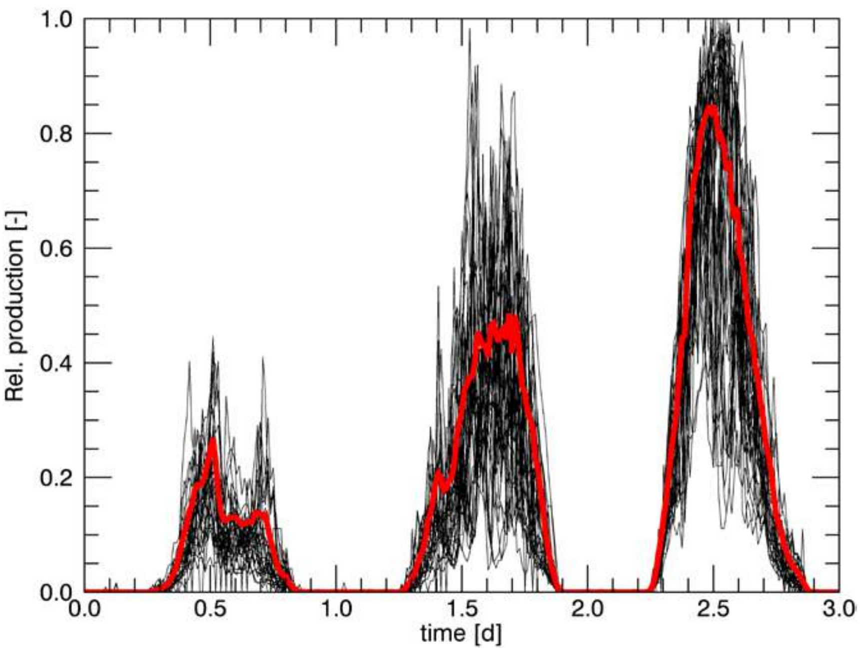

Figure 4.5: Geographical smoothing effect shown for 15 minute PV production data for Bern (90 installations).

Figure 4.6 show the dependence of correlation with distance between the locations for 15 minutes and 60 minutes averages.

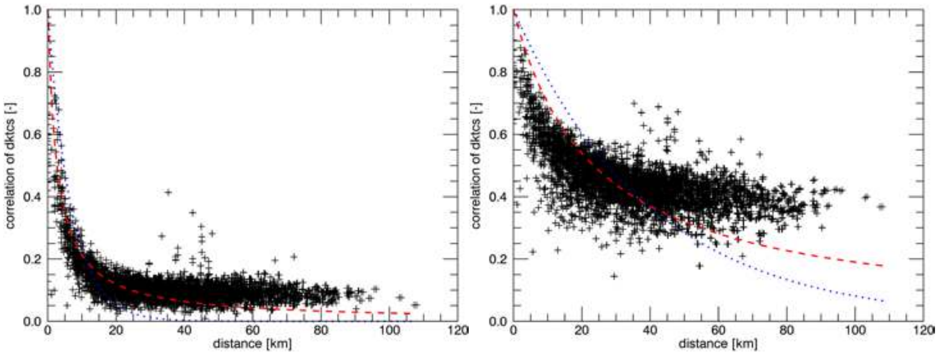

Figure 4.6: Correlation coefficients vs. distance for Bernese data. Left: 15 minute resolution, right: 1 hour resolution. Red line shows eq. 3.7, blue line eq. 3.8

The effect of time averaging is also in this case clearly visible. The correlations for 15 minute measurements are lower than 0.25 at 8 km. The threshold for one hour data for the correlation lower 0.25 is reached at 70 km (Table 4.2). For Energiepool Switzerlands' data of Bern the hyperbolic model (Eq. 3.7) shows a better fit.

Figure 4.7 shows the dependency of threshold distance with a correlation of <0.25 on the time resolution.

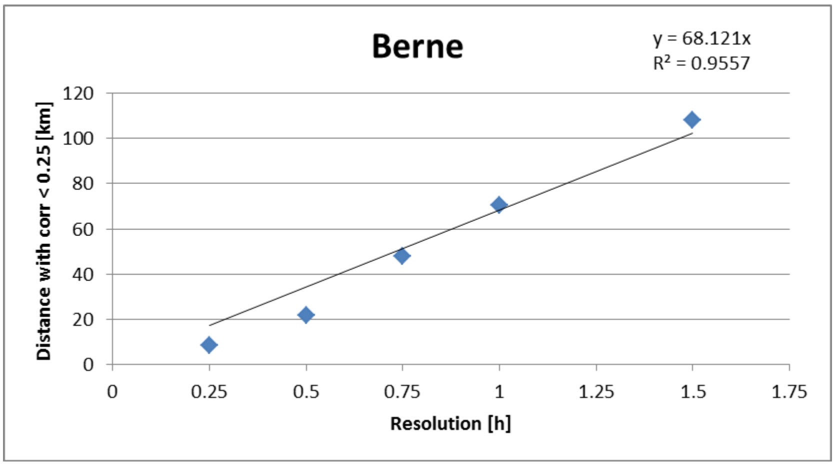

Figure 4.7: Distance with correlation < 0.25 vs. time resolution for Bern (hyperbolic model).

The relationship for Bern data is linear. The average cloud speed approximately 20 km/h.

4.1.3. Distributed generation – Switzerland

The DFM was applied to a network of 115 global radiation measurements. The source of the data is the Swissmetnet of MeteoSwiss. The data is available in one hour resolution.

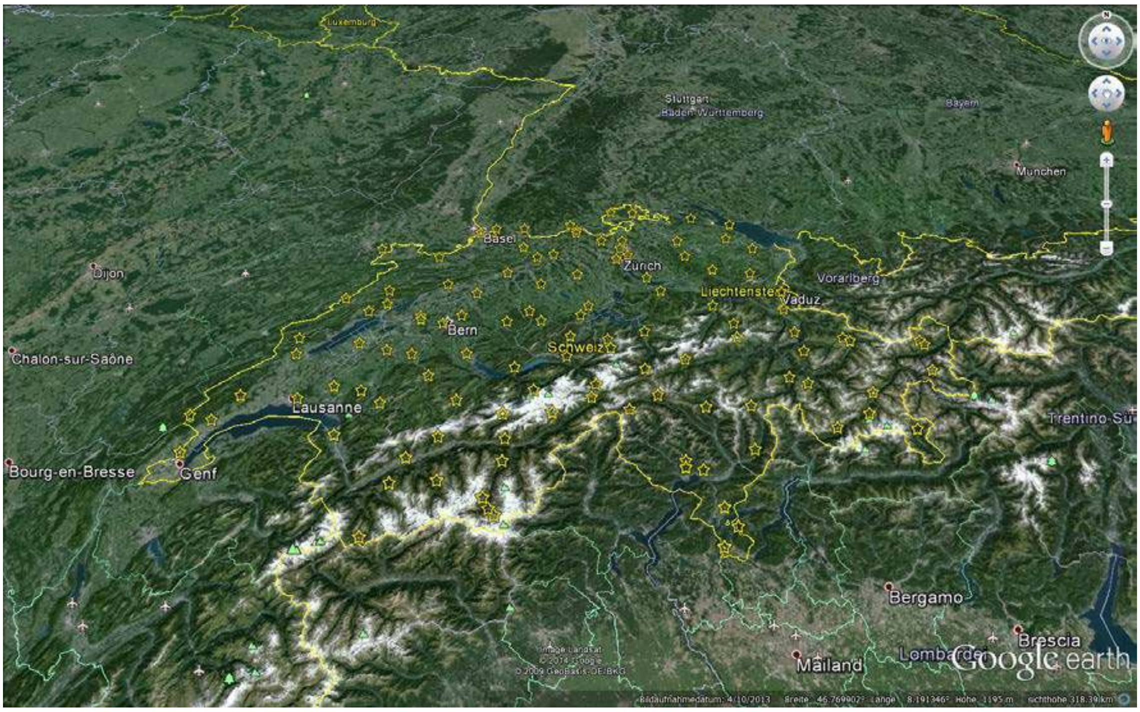

Figure 4.8: Global radiation network used for Switzerland.

We analyzed the period of July 2013 and the time resolution from 60 till 240 minutes. Figure 4.9 show the dependence of correlation with distance between the locations for 60 minutes and 120 minutes averages.

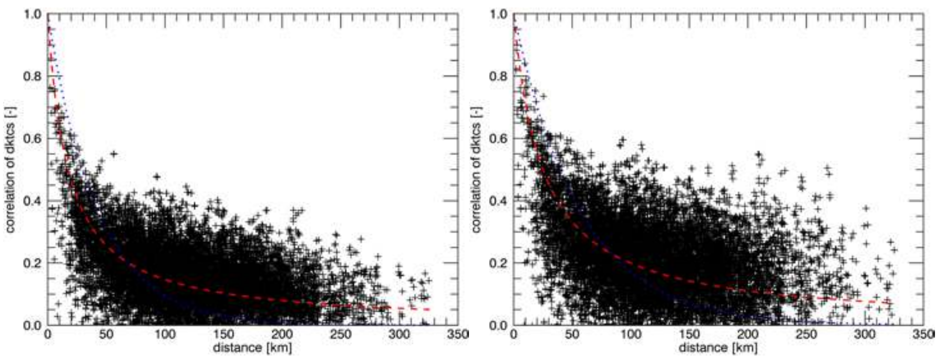

Figure 4.9: Correlation coefficients vs. distance for Swiss data. Left: 1 hour resolution, right: 2 hours resolution. Red line shows eq. 3.7, blue line eq. 3.8

The effect of time averaging is also in this case also visible – but less clear than for higher time resolutions. The correlations for one hour measurements are lower than 0.25 at 52 km. The threshold for two hour data for the correlation lower 0.25 is reached at 75 km (Table 4.2). For Swiss data the eq. 3.7 and 3.8 show a similar fit. The correlations vary to a great extent, which may be caused by the climatic effects of the Alps (separating the climate and the drift of the clouds).

Figure 4.10 shows the dependency of threshold distance with a correlation of <0.25 on the time resolution.

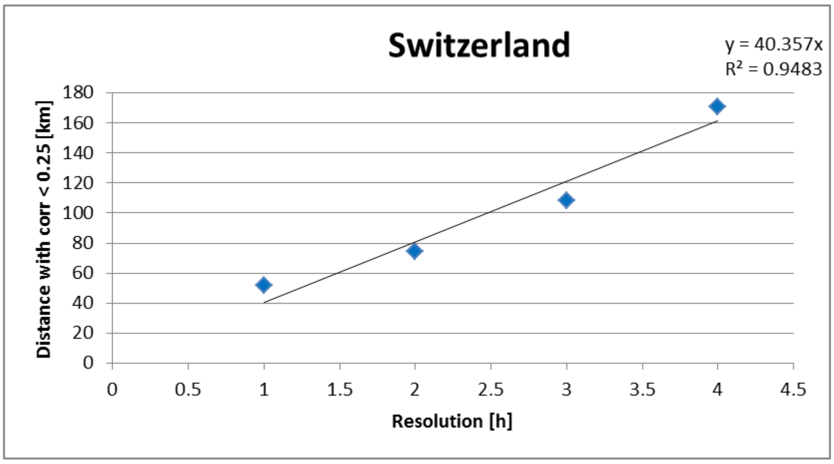

Figure 4.10: Distance with correlation < 0.25 vs. time resolution for Switzerland (hyperbolic model).

The relationship is relatively linear. The values at 60 minutes are similar to the one in the Canton of Bern. The average cloud speed is approximately 15 km/h.

7

4.1.4. Distributed generation – UK

The DFM was applied to a network of 18 global radiation measurements. The source of the data is UK metoffice – distributed over Ogimet (www.ogimet.com). The data is available in one hour resolution.

Figure 4.11: Global radiation network used for UK.

We analyzed the period of January - December 2013 and the time resolution from 60 till 240 minutes. Figure 4.12 show the dependence of correlation with distance between the locations for 60 minutes and 120 minutes averages.

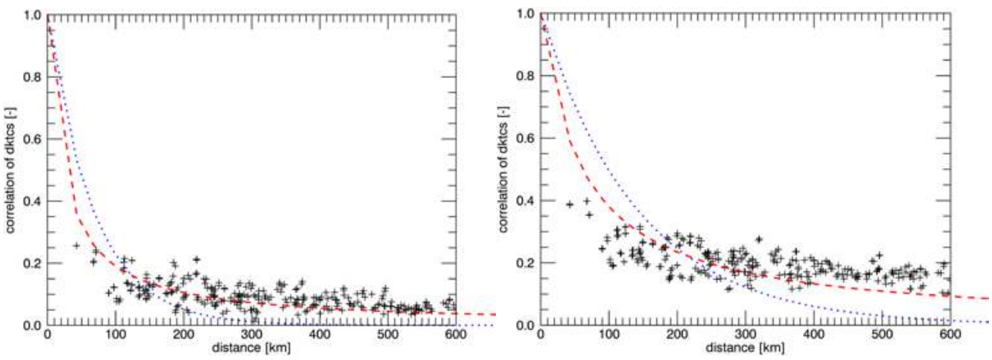

Figure 4.12: Correlation coefficients vs. distance for UK data. Left: 1 hour resolution, right: 2 hours resolution. Red line shows eq. 3.7, blue line eq. 3.8

The effect of time averaging is also in this case also visible. The correlations for one hour measurements are lower than 0.25 at 71 km. The threshold for two hours data for the correlation lower 0.25 is reached at 185 km (Table 4.2). For UK metoffice data the hyperbolic model shows a better fit.

Figure 4.13 shows the dependency of threshold distance with a correlation of <0.25 on the time resolution.

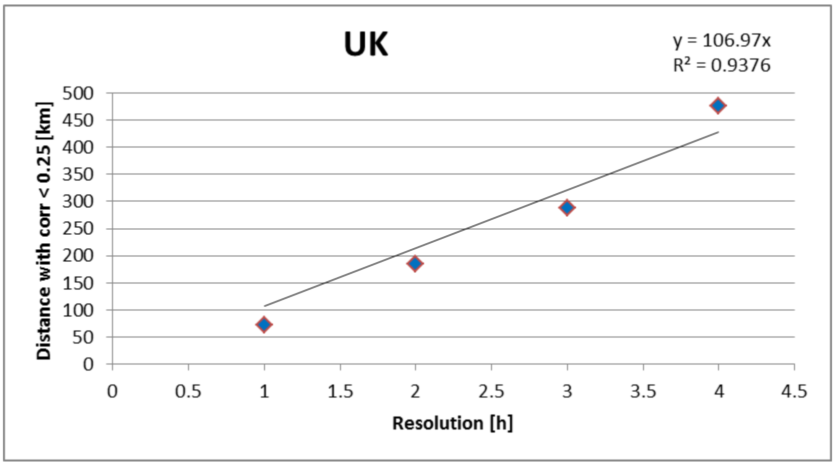

Figure 4.13: Distance with correlation < 0.25 vs. time resolution for UK data (hyperbolic model).

The relationship is quite linear and highest among the six example regions. Also the distances are highest, which is induced by high wind speed over UK. The average cloud speed is approximately 30 km/h.

4.1.5. Distributed generation – Southern Great Plaines, USA

The DFM was applied to a network of 12 global radiation measurements. The source of the Southern Great Plains (SGP) data is ARM (http://www.arm.gov/sites/sgp). The data is available in one minute resolution.

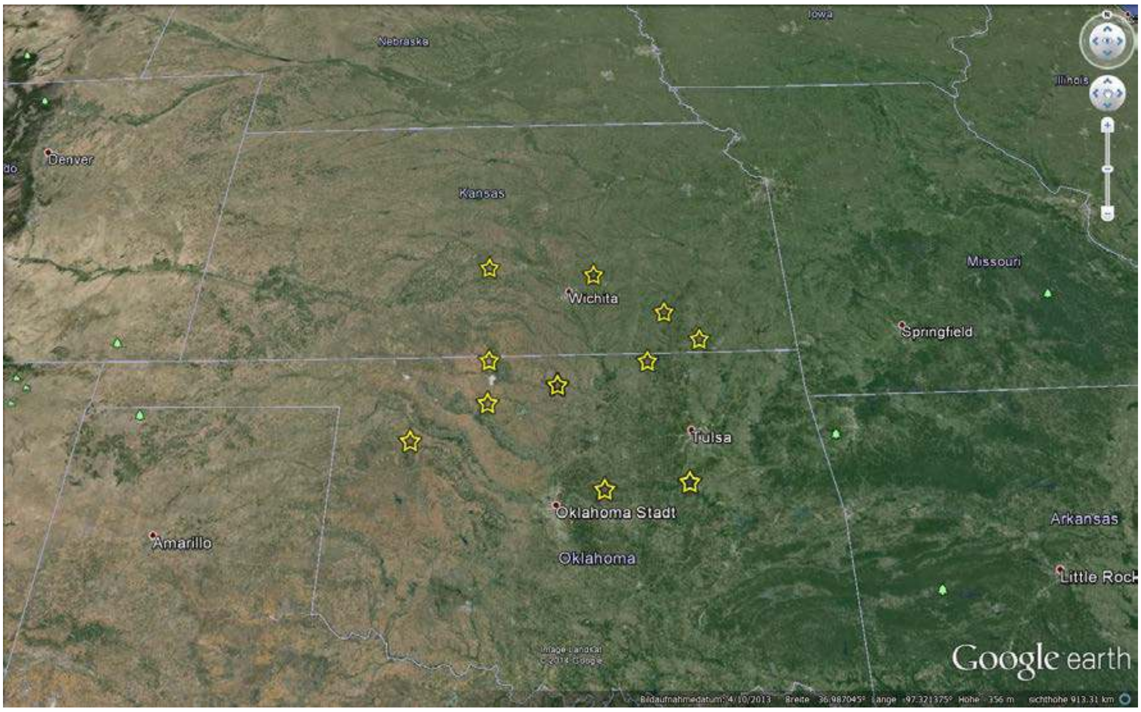

Figure 4.14: Global radiation network used for Southern Great Plaines (SGP), USA.

We analyzed the period of April and July 2011 and the time resolution from 2 minutes till 240 minutes. Figure 4.15 show the dependence of correlation with distance between the locations for 60 minutes and 120 minutes averages.

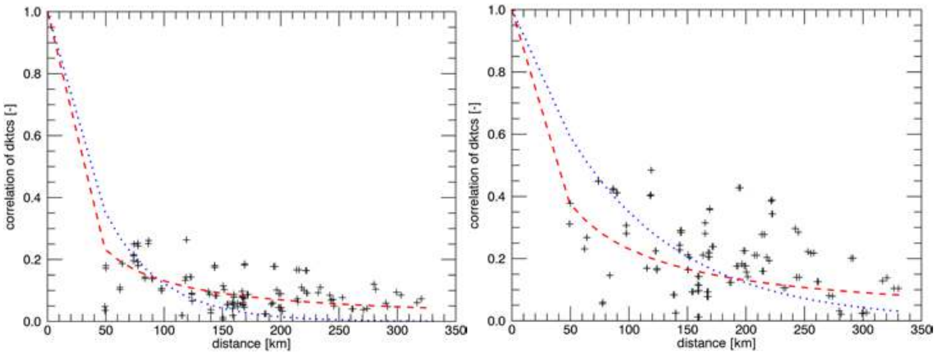

Figure 4.15: Correlation coefficients vs. distance for SGP data. Left: 1 hour resolution, right: 2 hours resolution. Red line shows eq. 3.7, blue line eq. 3.8

The effect of time averaging is also in this case also visible – but less clear than for higher time resolutions. The correlations for one hour measurements are lower than 0.25 at 49 km (the nearest distance between two locations). The threshold for two hours data for the correlation lower 0.25 is reached at 115 km (Table 4.2). For SGP data the exponential and the hyperbolic model shows an equal fit.

Figure 4.16 shows the dependency of threshold distance with a correlation of <0.25 on the time resolution.

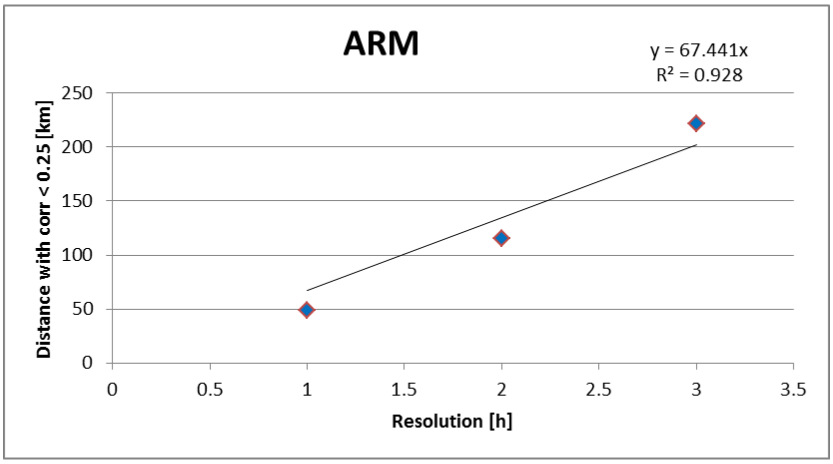

Figure 4.16: Distance with correlation < 0.25 vs. time resolution for SGP data (hyperbolic model).

The relationship is quite linear and highest among the six example regions. Also the distances are highest, which is induced by high wind speed over SGP. The average cloud speed is approximately 50 km/h.

4.1.6. Distributed generation – Japan

The DFM was applied to a network of 9 global radiation measurements. The source of the data is AIST. The data is available in one minute resolution.

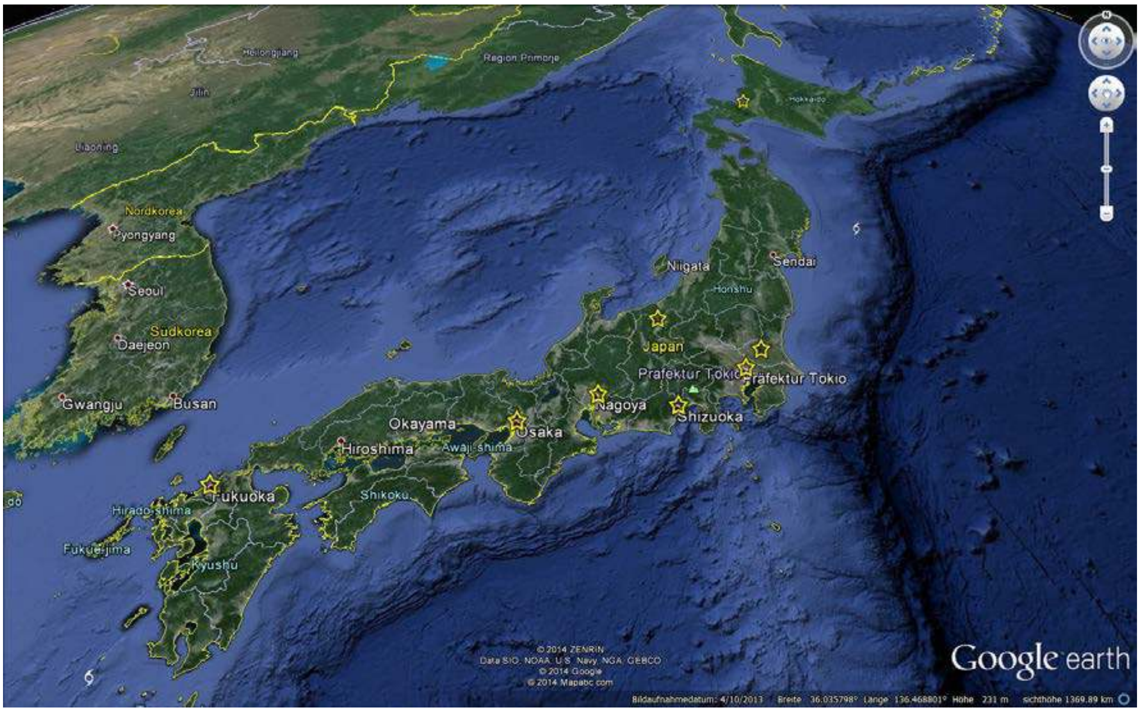

Figure 4.17: Global radiation network used for Japan.

We analyzed the period of January - December 2013 and the time resolution from 1 minute till 240 minutes. Figure 4.18 show the dependence of correlation with distance between the locations for 60 minutes and 120 minutes averages.

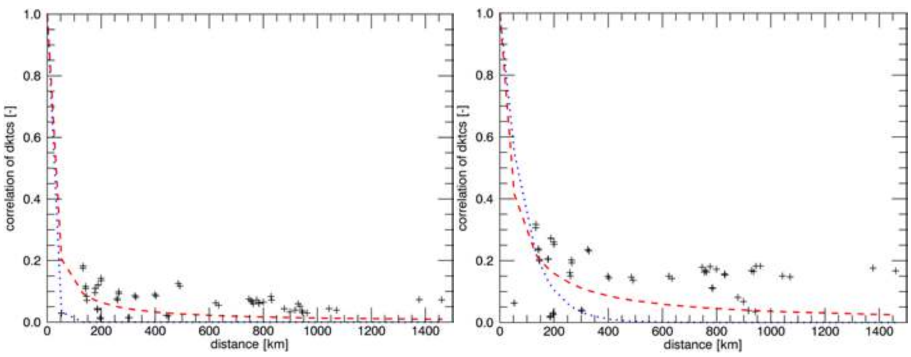

Figure 4.18: Correlation coefficients vs. distance for Japanese data. Left: 1 hour resolution, right: 2 hours resolution. Red line shows eq. 3.7, blue line eq. 3.8

The effect of time averaging is also in this case also visible. The correlations for one hour measurements are lower than 0.25 at 50 km. The threshold for two hours data for the correlation lower 0.25 is reached at 130 km (Table 4.2). For SGP data the exponential model shows a better fit.

Figure 4.19 shows the dependency of threshold distance with a correlation of <0.25 on the time resolution.

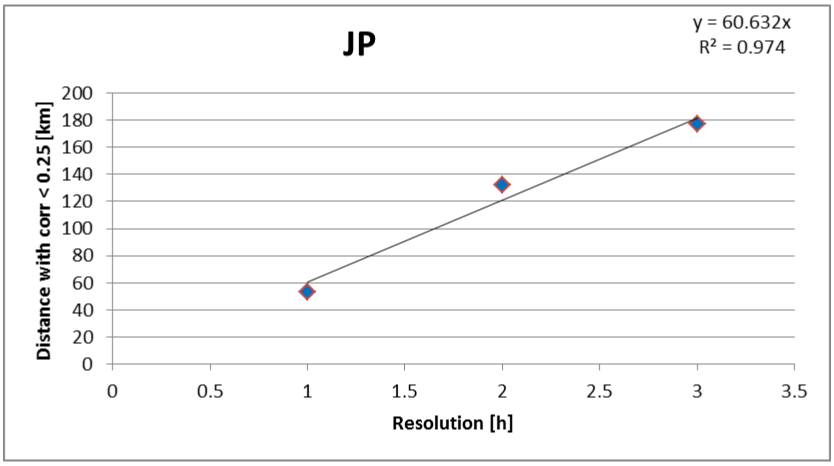

Figure 4.19: Distance with correlation < 0.25 vs. time resolution for Japan (hyperbolic model).

The relationship is quite linear and highest among the six example regions. Also the distances are highest, which is induced by high wind speed over SGP. The average cloud speed is approximately 38 km/h.

4.1.7. Overview of all six regions

Table 4.2 hows the parameters for Equations 3.7 and 3.8 and the calculated thresholds of distances with correlations lower than 0.25 as well as the variability reduction (VR) and the dispersion factor (L).

Table 4.2: Model coefficients of equations 3.7 and 3.8 and distances with correlation of < 0.25. Sdv. Δkc= standard deviation of ramps. VR = variability reduction (average of all sites); D = dispersion factor.

Location	Time resolution	Sdv. Δkc	VR	CS_1 Eq. 3.7 [km/h]	Distance Eq 3.7 corr. < 0.25 [km]	CS_2 Eq. 3.8 [km/h]	Distance Eq. 3.8 corr. < 0.25 [km]	D
Oahu	1 sec.	0.019	3.9	10.3	0.086	123.5	0.086	350
Oahu	15 sec.	0.099	2.7	4.1	0.086	18.3	0.099	59
Oahu	30 sec.	0.124	2.1	4.5	0.111	14.9	0.160	27
Oahu	1 min.	0.149	1.6	4.9	0.245	12.3	0.265	12
Oahu	2 min.	0.171	1.3	4.1	0.410	8.7	0.376	7
Oahu	3 min.	0.184	1.2	3.7	0.549	7.3	0.481	5
Bern	15 min.	0.091	2.5	10.9	8.2	29.3	9.5	18
Bern	30 min.	0.125	1.8	14.5	21.7	34.5	22.3	7
Bern	60 min.	0.173	1.3	23.5	70.4	42.7	55.1	2
Switzerland	1 hour	**0.210**	1.8	17.3	51.8	45.7	59.0	14
Switzerland	2 hours	0.266	1.6	12.5	74.7	30.5	78.7	10
Switzerland	3 hours	0.333	1.2	12.1	104	26.9	104	7
UK	1 hour	**0.209**	1.3	23.7	71.0	72.7	97.2	15
UK	2 hours	0.267	1.1	30.7	185	76.5	199	6
UK	3 hours	0.296	1.0	31.9	288	72.1	280	4
SGP	2 min.	0.115	2.7	-	-	-	-	13
SGP	1 hour	**0.236**	1.4	50.3	49.2	15.1	73.8	5
SGP	2 hours	0.249	1.5	49.3	115	23.3	115	2
SGP	3 hours	0.297	1.0	49.9	222	24.5	194	2
Japan	1 min.	0.074	2.5	-	-	-	-	25
Japan	1 hour	**0.246**	1.4	16.7	52.8	13.0	52.8	30
Japan	2 hours	0.288	1.2	47.7	132	38.1	132	5
Japan	3 hours	0.308	1.2	43.1	177	54.6	177	4

The Hawaii site shows high temporal variability with low wind speed. Switzerland and UK show lower variability, but higher wind speeds (especially UK). The variability reduction of the fleet (VR) is similar for most locations and is in the range of 1.0 – 3.9. The reduction gets clearly lower with longer averaging time periods. The standard deviations of the individual ramps show the following ranges (see also chapter 4.1.8):

- for one minute data, the values are between 0.074 (Japan) and 0.149 (Hawaii)
- for one hour data, the values are between 0.173 (Bern) and 0.246 (Japan)

The overall results are in accordance with the ones presented in Perez and Hoff [1], where gradients of correlation distances over time resolution between 15 h/km (Hawaii) and

40 h/km (Southern Great Planes) have been found. As assumed in that paper gradients are linear to a great extent. A slight lowering of the gradients at higher time resolutions is visible at some regions. This effect may be induced by the clustering of clouds to frontal systems, which move at lower speeds. Additionally the gradients and the cloud speed are proportional to each other (Figure 4.20). A general factor of 1.4 has been found at the six locations.

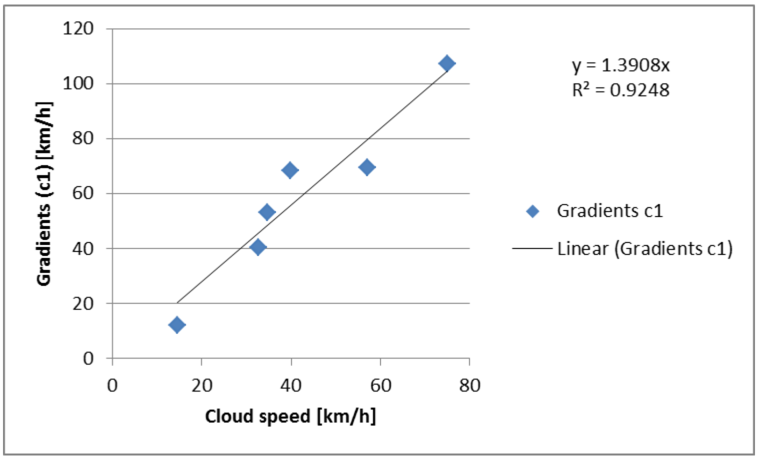

Figure 4.20: Gradients (of cloud speed 1 = c1 / hyperbolic model) vs. cloud speed

The outliers for the cloud speed values for 1 second data at Hawaii (123.5 km/h for c_2) are an example of inadequate space-time relation. The distances between the nearest locations (90 m) are too big for one second data. Additionally the time resolution of one minute or even one hour is too low for the Japan case which large distances. Based on Eq. 3.7, the possible range of cloud speed (12 – 44 km/h) and the correlation levels of 0.1 and 0.25 adequate space-time relations based on the distance with correlation < 0.1 can be determined (Table 4.3). Two PV installations with a distance larger than the adequate distance are independent (to a great extent) and therefore the fleet variability follows Eq. 2.2.

Table 4.3: Adequate time and space scales based on the distances with correlation < 0.1 – 0.25 and cloud speeds between 12 and 44 km/h. The found range is based on the values of the six analyzed regions.

Time resolution	Found range [corr. < 0.25] [km]	Adequate distances averages [km]	Adequate distance ranges [km]
1 sec.	-	0.05	0.01 – 0.11
15 sec.	0.09	0.19	0.04 – 0.4
1 min.	0.3	2.8	0.6 – 7
2 min.	0.4	5.6	1 – 13
5 min.	0.7	14	3 – 33
15 min.	8	42	9 – 99
30 min.	22	84	18 – 198
1 hour	50 – 70	168	36 – 396
2 hours	75 – 185	336	72 – 792
3 hours	100 - 290	504	108 – 1188

To give some reading examples of this table: for one minute values locations are only slightly correlated anymore in a distance of more than 0.6 – 7 km. For example using data with a spatial resolution of 0.1 km, all locations will be highly correlated. Using data with a spatial resolution of 20 km for one minute time resolution the correlation will be almost zero. For 15 minute data no correlation will be reached with spatial resolutions of 100 km or more and high correlations for resolutions of 5 km or lower.

4.1.8. Global model for spatial smoothing

In a last step we try to obtain a simple global model for spatial smoothing and PV fleet behavior. Equations 3.7 and 3.8 can be used to model these topics. Therefore two parameters – the standard deviation of the individual ramps and the cloud speed – have to be known globally.

The temporal variability of 10 minute and 1 hour **ramps** have been analyzed at 20 BSRN sites throughout the world. The best dependency could be obtained by classifying the values in three different main climate zones of Köppen-Geiger (Figure 4.21) [27].

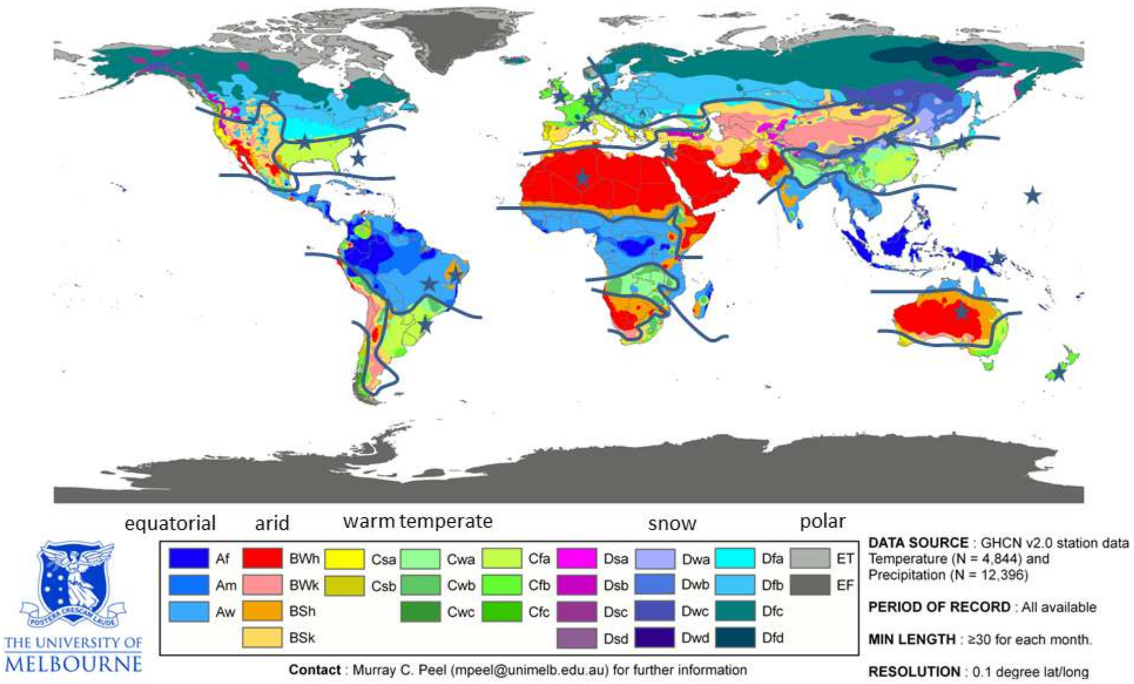

Figure 4.21: Climate zones definition of Köppen-Geiger with three main classes "equatorial" (blue), arid (red) and temperate (yellow-green-magenta) and the 20 analyzed BSRN sites (stars).

Three groups have been determined: equatorial, arid and warm temperate zones (Regina lies in the snow zone, but has been classified in the warm temperature zone).

Figure 4.22 shows the box plots of the found variability. One hour ramps are generally 1.5 times higher than 10 minute ramps (scaled to the same time unit however 4 times less!).

The variability is highest in equatorial, mid in temperate zones (with a greater range) and lowest in arid zones (mainly desert locations). The values found at the 6 test regions are similar to the values calculated at the BSRN sites. The median values of the standard deviation of the 1 hour ramps lie at 0.17 for arid areas, 0.25 for equatorial areas and 0.22 for temperate. The corresponding values of 10 minute values are 0.11, 0.17 and 0.13.

Another possibility to model the variability worldwide would be to use dominant cloud type and link it to variability as Stein and Reno [28] did. However as cloud type information is not available worldwide (but only for USA) this option couldn't be investigated within this case study.

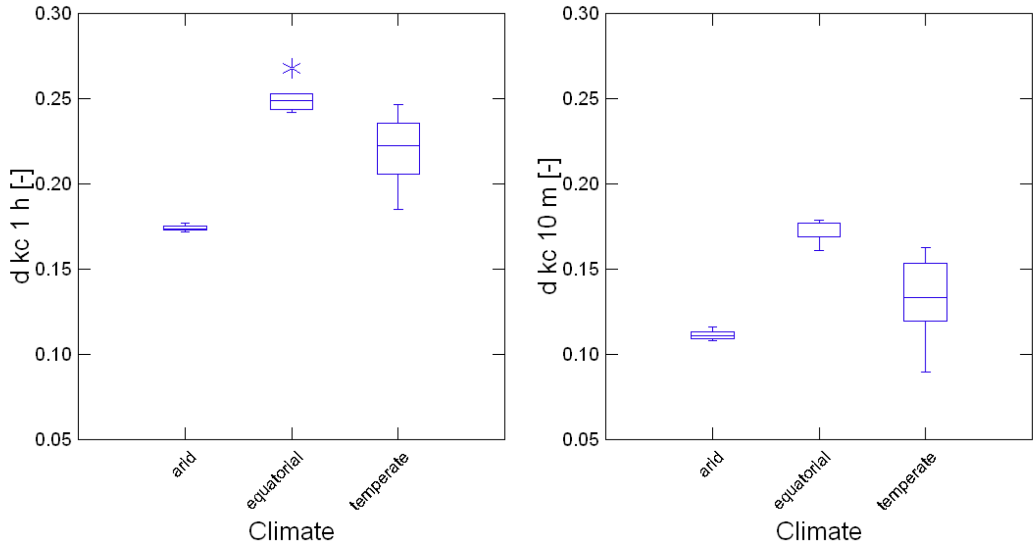

Figure 4.22: Box plots of standard deviation of and 1 hour (left) and 10 minute (right) relative ramps at 19 BSRN sites based on climate zones (Köppen-Geiger).

The average cloud speed can be determined using the average wind speed at 700 hPa (approximately at 3 km altitude), which is the most important level for cloud transport (Kühnert, 2013 [29]).

Figure 4.23 shows the average wind speed at 700 hPa based on NCEP [30] reanalysis data (average from 1948 – 2013). The cloud speed parameter varies worldwide between 5 and 70 km/h, the average is at 24 km/h and the median 20 km/h. 10% quantile comes to 13 km/h and 90% quantile to 44 km/h.

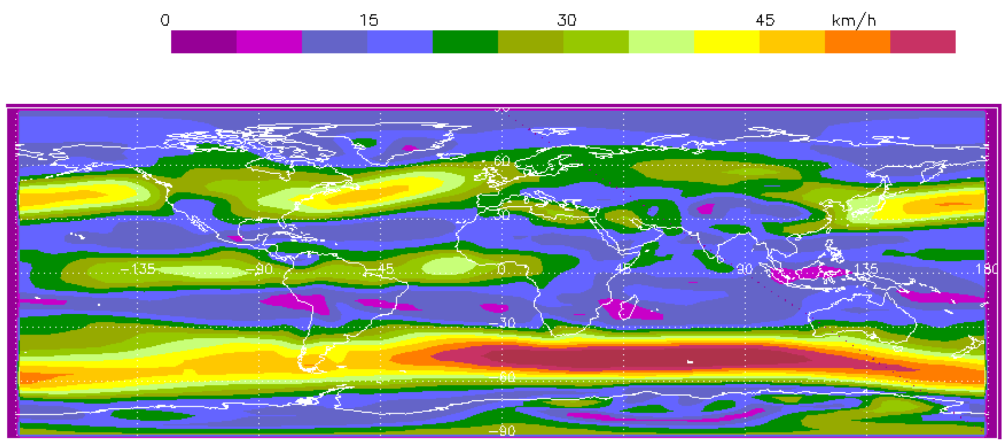

Figure 4.23: Average wind speed of NCEP reanalysis (1948 - 2013) at 700 hPa in km/h.

For the five test regions (Hawaii, Switzerland, UK, SGP and Japan) the cloud speed values (4, 14, 31, 19 and 42 km/h respectively) are similar to the reanalysis values (13, 19, 27, 26 and 39 km/h). NCEP cloud speeds are slightly higher for Hawaii and Switzerland, where most presumably rough topography is the reason for lower wind speeds.

Like this the two parameters can be determined, which allows to model the smoothing effects without detailed measurements.

4.2. Wavelet Variability Model

To demonstrate the Wavelet Variability Model the distributed sensor system in Oahu, Hawaii, USA will be used (Figure 4.1: Sensor grid in Oahu, Hawaii, USA.).

The variability of the point sensor, the simulated power plant and the actual power plant will be compared based on the power content of each signal, at each timescale. The power of a wavelet mode $w_{\bar{t}}(t)$ is defined as:

$$\mathrm{P_s}(\bar{t}) = \frac{1}{T}\int |w_{\bar{t}}(t)|^2 dt \qquad (4.1)$$

Since the $\mathrm{P_s}$ describes the variability content rather than the time of occurrence, it allows measuring the accuracy of the WVM independent of geographic limitations.

4.2.1. Distributed generation

The WVM was applied to a distributed system owned by the National Renewable Energy Laboratory (NREL), located in Oahu, Hawaii, USA (Figure 4.1). The system consists of a 17 global horizontal irradiance sensor grid (data available online [4]) spread across approximately 0.76 km², with high resolution (1 reading per second). Temperature readings are also available.

Since the system only comprises sensors, PV power production was simulated using a simple diode model. The following parameters (from Centrosolar S 220P54 Excellent) were used to perform the calculations:

Table 4.4: Centrosolar S 220P54 Excellent module characteristics under standard test conditions.

Rated output (W)	220
Short-circuit current (A)	8.78
Open-circuit voltage (V)	32.89
Voltage (V)	27.26
Current (A)	8.07
NOCT (°C)	46
Number of cells	54

In this case, since several irradiance sensors were available, the scaling factor A was calculated based on the readings six of these sensors on the 23rd of August 2010, resulting in a value of 3.73. The derate factor of the entire system was calculated based on the average temperature of the period of analysis, the average irradiance of the period of analysis and the thermal coefficient of the panel's power output (-0.45%/°C), resulting in a value of 0.91. The power content of each timescale of one point sensor, the WVM simulated power plant and the diode model simulated power plant is presented in Figure 4.24.

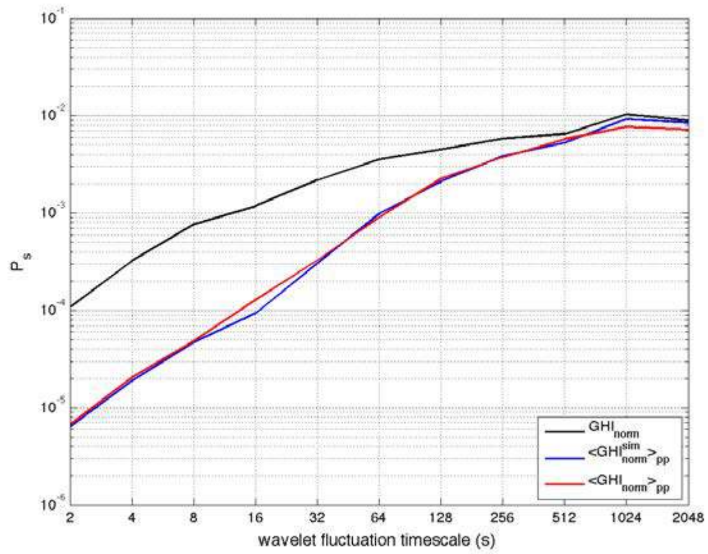

Figure 4.24: Power content of the GHI point sensor (black), actual power output (red) and simulated power output (blue) on August 23, 2010.

In the figure, the black line corresponds to the power content of the fluctuations of the single GHI point sensor, while the red line corresponds to the power content of the fluctuations of the whole system power output using the diode model. The figure confirms that the fluctuations that occur at a shorter timescale are the ones that are more reduced due to geographic smoothing. Fluctuations longer than 512 s (approximately 8.5 minutes) virtually do not benefit from the smoothing effect. The figure also shows that there is a good agreement between WVM simulated (blue line) and diode model output power content, thus validating the proposed method.

Figure 4.25 shows the variability reduction at each timescale. In the same line of thought, the variability reduction of fluctuations at long timescales is nearly 1, which means that there is no reduction. The shortest timescales have a variability reduction of 17, which is the number of sensors (panels) considered in the analysis.

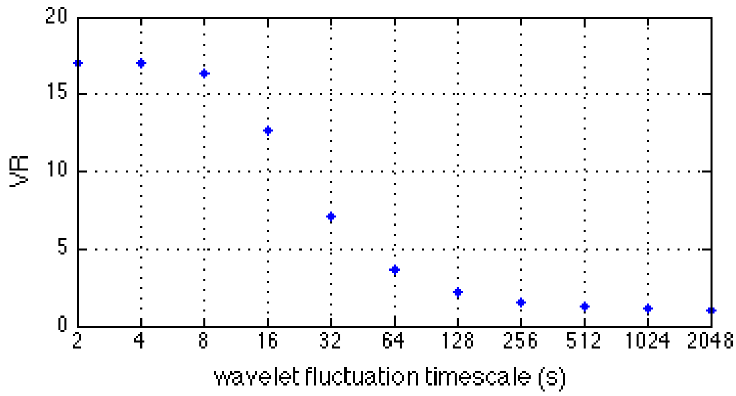

Figure 4.25: Variability reduction at each timescale.

5. Conclusions

The increasing penetration of PV systems in the distribution network raises several issues for the grid operation. New challenges must be tackled in order to keep a stable and balanced power grid. In this work, special emphasis was given to the variability associated with PV systems.

In chapter 2, the problems associated with PV variability were explained and it was shown that irradiance fluctuations of a single point can be very significant and fast. However, this issue can be minimized taking into account that the variability of a single PV system is highly reduced when, instead, a fleet of PV systems is considered. That is called the "smoothing effect".

In chapter 3, mainly three different variability models were presented. In the first one (representative blocks), the amplitude of the fluctuations was the main focus and information about the duration of the fluctuations was not considered. The second method (dispersion factor) focuses on the variability itself, but its data requisites were very demanding, which can be a hindrance. The third and final method (wavelet analysis) proved to be a good choice since it needs very limited data inputs and it is able to decompose the input irradiance signal into different timescales of fluctuations. By doing this, the variability reduction can be accessed and calculated separately for each timescale.

In chapter 4, seven case studies were presented: six for the Dispersion Factor Model (DFM) in different regions and with different time and space resolution and one of a distributed generation system in Hawaii, USA.

The results for the DFM are in good accordance with the ones presented in Perez and Hoff [1]. The hyperbolic function fits better for most test cases. The variability of the ramps could be linked to climate zones. The found cloud speeds are also similar to climatological wind speed averages at 700 hPa based on reanalysis data. The two links allows to model time-space correlations also without measurements for every location in the world.

In the wavelet model case study for Oahu the smoothing effect had a higher impact on fluctuations occurring in timescales lower than 512 seconds (approximately 8.5 minutes), with fluctuations above those timescales remaining practically the same. In the Hawaii site, comparing the power content of the power output of the system using a diode model and the wavelet method simulation, a very good agreement was observed. The wavelet method is able to predict with high reliability the variability reduction at each timescale.

The current report shows the general validity of the models and suggests a simple global model for modelling variability of PV fleets. Both need further validations at more sites and in more regions to detect the strengths and limitations of the models and the worldwide usability.

Acknowledgements

We like to thank the National Renewable Energy Laboratory (NREL) to use their Oahu solar measurement grid data, Energiepool Switzerland AG to let us analyze their PV production data of Canton of Bern, UK metoffice to use radiation data of 18 stations, U.S. Department of Energy as part of the Atmospheric Radiation Measurement (ARM) Climate Research Facility to use global horizontal radiation data of 12 sites and AIST to let us use data of 8 Japanese sites of JMA. Additionally we thank the World Radiation Monitoring Center (WRMC) for the data of 20 BSRN stations.

References

[1] T. E. Hoff and R. Perez, “Modeling PV Fleet Output Variability,” *Solar Energy, Vol. 86,* pp. 2177-2189, 2011.

[2] BGR, Energiestudie 2013. Reserven, Ressourcen und Verfügbarkeit, Hannover, 2013.

[3] IEA PVPS, "2014 - Snapshop of Global PV Markets," Report IEA PVPS T1-26:2015, 2015.

[4] NREL Measurement and Instrumentation Data Center. [Online]. Available: http://www.nrel.gov/midc/kalaeloa_oahu/. [Accessed 27 June 2013].

[5] M. Eddy, "Solar Eclipse and Supermoon Have Europe Energy Providers Watchful," *The New York Times,* no. March 20, 2015, p. 1, 2015.

[6] IEA, The power of transformation, Paris: IEA, 2014.

[7] M. Lave, J. Kleissl and E. Arias-Castro, “High-frequency irradiance fluctuations and geographic smoothing,” *Solar Energy,* vol. 86, no. 8, pp. 2190-2199, 2012.

[8] A. E. Curtright and J. Apt, “The character of power output from utility-scale photovoltaic systems,” *Progress in Photovoltaics,* vol. 16, pp. 241-247, 2008.

[9] M. Lave and J. Kleissl, “Solar variability of four sites across the state of Colorado,” *Renewable Energy,* vol. 35, pp. 2867-2873, 2010.

[10] T. E. Hoff and R. Perez, “Quantifying PV power Output Variability,” *Solar Energy,* vol. 84, pp. 1782-1793, 2010.

[11] T. Kato, T. Inoue and Y. Suzuoki, “Estimation of Total Power Output Fluctuation of High Penetration Photovoltaic Power Generation System,” in *Proc. IEEE Power and Energy Society General Meeting*, Detroit, Michigan, USA, 2011.

[12] A. Mills and R. Wiser, “Implications of Wide-Area Geographic Diversity for Short-Term Variability of Solar Power,” LBNL Report 3884E, 2010.

[13] R. Perez and T. E. Hoff, "Mitigation short-term PV output intermittency," in *28th EU PVSEC*, Paris, 2013.

[14] R. Perez, *IEA SHC Task 46 meeting La Reunion; Presentation of subtask A,* Saint-Pierre, La Reunion, 2014.

[15] M. Lave, J. Kleissl and J. S. Stein, “A Wavelet-Based Variability Model (WVM) for Solar PV Power Plants,” *submitted to IEEE Transactions on Sustainable Energy Special Issue on Solar Energy,* 2011.

[16] M. Lave, J. S. Stein and A. Ellis, "Analyzing and Simulating the Reduction in PV Powerplant Variability Due to Geographic Smoothing in Ota City, Japan and Alamosa, CO," in *IEEE 38th Photovoltaic Specialists Conference (PVSC)*, 2012.

[17] M. Lave and J. Kleissl, "Cloud Speed Impact on Solar Variability Scaling - Application to the Wavelet Variability Model," *Solar Energy,* vol. 91, pp. 11-21, 2013.

[18] R. Perez, P. Ineichen, E. Maxwell and R. Seals, "Dynamic Global-To-Direct-Irradiance Conversion Models," *ASHREA Transactions: Research,* pp. 354-369, 1992.

[19] A. Skartveit and J. Olseth, "The probability density and autocorrelation of short-term global and beam irradiance," *Solar Energy,* pp. 477-487, 6 49 1992.

[20] J. Stein, M. Reno and C. Hansen, "THE VARIABILITY INDEX : A NEW AND NOVEL METRIC FOR QUANTIFYING IRRADIANCE AND PV OUTPUT VARIABILITY," in *ASES 2012*, 2012.

[21] A. Woyte, R. Belmans and J. Nijs, “Power Flow Fluctuations in Distribution Grids with High PV Penetration,” in *Proc. 17th European Photovoltaic Solar Energy Conference and Exhibition*, Munich, Germany, 2001.

[22] P. Ineichen, "A broadband simplified version ot the Solis clear sky model," *Solar Energy,* vol. 82, no. 8, pp. 758-762, 2008.

[23] R. W. Müller, K. F. Dagestad, P. Ineichen, M. Schroedter, S. Cros, D. Dumortier, R. Kuhlemann, J. A. Olseth, C. Piernavieja, C. Reise, L. Wald and D. Heinemann, "Rethinking satellite based solar irradiance modelling – the SOLIS clear sky module," *Remote Sens. 91,* pp. 160-174, 2004.

[24] J. Page, “The role of solar radiation climatology in the design of photovoltaic systems,” in *Pratical handbook of photovoltaics: fundamentals and applications*, Elsevier, 2003, pp. 5-66.

[25] B. Ridley, J. Boland and P. Lauret, “Modelling of diffuse solar fraction with multiple predictors,” *Renewable Energy,* vol. 35, no. 2, pp. 478-483, 2010.

[26] R. Perez, R. Stewart, C. Arbogast, R. Seals and J. Scott, "An anisotropic hourly diffuse radiation model for sloping surfaces: description, performance, validation, site dependency evaluation," *Solar Energy, Vol. 36, No. 6,* pp. 481-497, 1986.

[27] M. Peel, B. Finlayson and M. McMahon, “Updated world map of the Köppen-Geiger climate classification,” *Hydrol. Earth Syst. Sci., 11,* pp. 1633-1644, 2007.

[28] J. Stein and M. J. Reno, "Using cloud classification to model solar variability," in *ASES*, Baltimore, 2013.

[29] J. Kühnert, *Short term forecasting based on satellite data: ECMWF winds as Cloud Motion Vectors,* Oldenburg, 2013.

[30] E. Kalnay, M. Kanamisu, R. Kistler and W. Collins, "The NCEP/NCAR 40-Year Reanalysis Project," *BAMS, Vol. 77, No. 3,* pp. 437-471, March 1996.

Glossary

Term	Definition
ARM	Atmospheric Radiation Measurement (Climate Research Facility)
BSRN	Baseline Surface Radiation Network, global high quality solar radiation network
CS	Cloud speed
DFM	Dispersion Factor Model
DSO	Distribution system operators
GHI (also G)	Global Horizontal Irradiance, shortwave radiation ($\lambda < 3$ μm), received by a horizontal surface from the solid angle 2π
kt	clearness index
ktcs	clear-sky clearness index
NREL	National Renewable Energy Laboratory
PV	photovoltaic solar energy
Ramp rate	Difference between two consecutive global radiation or PV values normalized by the clear-sky radiation or the installed peak power corrected for the solar azimuth
TSO	Transmission system operator
WVM	Wavelet variability model

ISBN 978-3-906042-35-0